

1 **NHE6-Depletion Corrects ApoE4-Mediated Synaptic Impairments and Reduces Amyloid**  
2 **Plaque Load**

3 Theresa Pohlkamp<sup>1,2\*#</sup>, Xunde Xian<sup>1,2,7\*</sup>, Connie H Wong<sup>1,2\*</sup>, Murat Durakoglugil<sup>1,2</sup>, Gordon C  
4 Werthmann<sup>1,2</sup>, Takaomi Saido<sup>8</sup>, Bret M Evers<sup>2</sup>, Charles L White<sup>4</sup>, Jade Connor<sup>1,2</sup>, Robert E  
5 Hammer<sup>3</sup>, Joachim Herz<sup>1,2,5,6,#</sup>

6

7 Author Information:

8 <sup>1</sup>Departments of Molecular Genetics, <sup>2</sup>Center for Translational Neurodegeneration Research,  
9 <sup>3</sup>Biochemistry, <sup>4</sup>Pathology, <sup>5</sup>Neuroscience, <sup>6</sup>Neurology and Neurotherapeutics, University of  
10 Texas Southwestern Medical Center, Dallas, TX 75390, USA; <sup>7</sup>Institute of Cardiovascular  
11 Sciences and Key Laboratory of Molecular Cardiovascular Sciences, Ministry of Education,  
12 Peking University, Beijing 100191, China; <sup>8</sup>Laboratory for Proteolytic Neuroscience, RIKEN  
13 Brain Science Institute, Wako-shi, Saitama, Japan.

14 \*These authors contributed equally to this work.

15 #Correspondence to:

16 [ThePohlkamp@gmail.com](mailto:ThePohlkamp@gmail.com) (T.P.), [Joachim.Herz@utsouthwestern.edu](mailto:Joachim.Herz@utsouthwestern.edu) (J.H.)

17

18

19 **Impact Statement:** Genetic disruption of sodium-hydrogen exchanger 6 (NHE6/*Slc9a6*)  
20 reduces amyloid plaques in humanized Alzheimer's disease mouse models and restores normal  
21 synaptic responses to neuromodulatory input in humanized ApoE4 expressing animals.

22

23

24

25 **ABSTRACT**

26           Apolipoprotein E4 (ApoE4) is the most important and prevalent risk factor for late-onset  
27 Alzheimer's disease (AD). The isoelectric point of ApoE4 matches the pH of the early  
28 endosome (EE), causing its delayed dissociation from ApoE receptors and hence impaired  
29 endolysosomal trafficking, disruption of synaptic homeostasis and reduced amyloid clearance.  
30 We have shown that enhancing endosomal acidification by inhibiting the EE-specific sodium-  
31 hydrogen exchanger 6 (NHE6) restores vesicular trafficking and normalizes synaptic  
32 homeostasis. Remarkably and unexpectedly, loss of NHE6 (encoded by the gene *Slc9a6*) in  
33 mice effectively suppressed amyloid deposition even in the absence of ApoE4, suggesting that  
34 accelerated acidification of early endosomes caused by the absence of NHE6 occludes the  
35 effect of ApoE on amyloid plaque formation. NHE6 suppression or inhibition may thus be a  
36 universal, ApoE-independent approach to prevent amyloid buildup in the brain. These findings  
37 suggest a novel therapeutic approach for the prevention of AD by which partial NHE6 inhibition  
38 reverses the ApoE4 induced endolysosomal trafficking defect and reduces plaque load.

39

## 40 INTRODUCTION

41 ApoE is the principal lipid transport protein in the brain. Three different ApoE isoforms are  
42 common in humans: ApoE2 ( $\epsilon$ 2), ApoE3 ( $\epsilon$ 3), and ApoE4 ( $\epsilon$ 4). Each ApoE4 allele reduces the  
43 age of Alzheimer's disease (AD) onset by approximately three to five years compared to ApoE3  
44 homozygotes, which comprise ~80% of the human population (Roses, 1994; Sando et al.,  
45 2008). By contrast and by comparison, ApoE2 is protective against AD (Corder et al., 1994;  
46 Panza et al., 2000; West et al., 1994). ApoE is an arginine-rich protein and a major component  
47 of very-low density lipoproteins (Shore and Shore, 1973). The number of positively charged  
48 arginine residues differs between the three human isoforms due to two single nucleotide  
49 polymorphisms in the ApoE gene. The most common isoform, ApoE3, has a charge neutral  
50 cysteine at amino acid position 112 and an arginine at position 158. The second most common  
51 isoform, ApoE4, has two arginines, while the less frequent ApoE2 has two cysteines at these  
52 respective positions. The positively charged arginines raise the net charge and thus the  
53 isoelectric point (IEP) of the protein. (Eto et al., 1985; Warnick et al., 1979). The IEP of ApoE2 is  
54 the lowest (5.9), ApoE3 has an intermediate IEP of 6.1 and the IEP of ApoE4 is ~6.4 (Ordovas  
55 et al., 1987).

56 For cargo delivery, ApoE binds to lipoprotein receptors and undergoes endocytosis and  
57 recycling. Endocytic subcompartments become progressively more acidic, and the pH of these  
58 compartments is regulated by the opposing functions of vesicular ATP-dependent proton pumps  
59 (vATPase) and proton leakage channels ( $\text{Na}^+/\text{H}^+$  exchangers, NHEs). Early endocytic vesicles  
60 are slightly acidic (pH, ~6.4), which facilitates ligand/receptor dissociation. Lysosomes are highly  
61 acidic (pH 4 to 5), which is required for the digestion of endocytosed biomolecules (**Figure 1A**)  
62 (Casey et al., 2010; Naslavsky and Caplan, 2018). For maturation of the early endosomes (EE)  
63 and entry into the next sorting stage, ligand/receptor dissociation is required. The pH-dependent  
64 release of ApoE from its receptor in the EE is important for endosomal maturation and cargo  
65 delivery (Yamamoto et al., 2008) for the ability of endosomal content to rapidly recycle to the cell  
66 surface (Heeren et al., 1999; Nixon, 2017). The early endosomal pH, which triggers ligand-  
67 receptor dissociation, closely matches the IEP of ApoE4 (Xian et al., 2018). Loss of net surface  
68 charge at the IEP is accompanied by reduced solubility in an aqueous environment, leading to  
69 impaired dissociation of ApoE4 from its receptors (Xian et al., 2018) and aided by a greater  
70 propensity of ApoE4 to form a molten globule configuration under acidic conditions (Morrow et

71 al., 2002). Dysregulation of endolysosomal trafficking by ApoE4 causes an age dependent  
72 increase in EE number and size (Nuriel et al., 2017).

73 Based on these observations, we have proposed a model in which destabilization of  
74 ApoE4 in the acidic EE environment, combined with a greater propensity for self-association,  
75 results in delayed detachment from its receptors (**Figure 1B**). Subsequent endosomal swelling  
76 through  $K^+$ ,  $Na^+$  and  $H_2O$  influx further impairs cargo delivery, receptor recycling, and ligand re-  
77 secretion. Importantly, in neurons, ApoE and its receptor Apoer2 travel together with glutamate  
78 receptors through the endosomal recycling pathway (Chen et al., 2010; Xian et al., 2018). Rapid  
79 endocytosis and subsequent recycling of synaptic receptors is triggered by the synaptic  
80 homeostatic modulator and Apoer2 ligand Reelin (Hiesberger et al., 1999; Trommsdorff et al.,  
81 1999). We previously showed that ApoE4, in contrast to ApoE3 and ApoE2, prevents Reelin-  
82 mediated glutamate receptor insertion at the synapse, a state we refer to as ApoE4-mediated  
83 Reelin resistance (Chen et al., 2010; Durakoglugil et al., 2009; Lane-Donovan and Herz, 2017;  
84 Lane-Donovan et al., 2014; Xian et al., 2018). Reduction of endosomal pH and increasing the  
85 differential to the ApoE4 IEP abolishes this effect *in vitro* (Xian et al., 2018).

86 The pH of EE compartments is controlled by the vATPase-dependent proton pump and  
87 proton leakage through NHE6 (Nakamura et al., 2005; Basu et al., 1976; Davis et al., 1987;  
88 Rudenko et al., 2002). NHE6 is encoded by the gene *Slc9a6*. We showed that EE acidification  
89 by pharmaceutical pan-NHE inhibition or selective NHE6/*Slc9a6* knockdown in neurons  
90 prevents the ApoE4-caused trafficking delay of ApoE and glutamate receptors (Xian et al.,  
91 2018). NHE6-deficiency in humans causes neurodevelopmental defects, which result in  
92 Christianson syndrome, an X-linked genetic disorder characterized by cognitive dysfunction,  
93 autism, ataxia, and epilepsy. However, some *Slc9a6* mutant variants causing Christianson  
94 syndrome in humans do not significantly alter the ion exchange properties of NHE6 (Ilie et al.,  
95 2020; Ilie et al., 2019) suggesting that Christianson syndrome could be caused by loss of NHE6  
96 scaffolding functions and not by loss of endosomal pH regulation. To investigate whether NHE6-  
97 depletion can reverse ApoE4 pathology *in vivo*, we generated a conditional *Slc9a6* knockout  
98 mouse line (*Slc9a6<sup>fl</sup>;CAG-Cre<sup>ERT2</sup>*) to avoid complications caused by neurodevelopmental  
99 defects by temporally and spatially controlling NHE6-ablation. We show that genetic NHE6-  
100 ablation attenuates both, the ApoE4 induced Reelin resistance and impaired synaptic plasticity  
101 in ApoE4 targeted replacement (*ApoE<sup>APOE4</sup>*) mice using hippocampal field recordings.

102 The pathological hallmarks of AD are extracellular aggregates of the amyloid  $\beta$  ( $A\beta$ )  
103 peptide and intracellular tangles of hyperphosphorylated tau protein. Processing of the  
104 transmembrane amyloid precursor protein (APP) at the  $\beta$ - and  $\gamma$ -sites leads to  $A\beta$  production.  
105  $A\beta$  forms neurotoxic oligomers and accumulates in plaques. The  $\beta$ -site amyloid precursor  
106 protein cleaving enzyme 1 (BACE1) cleaves APP in its extracellular juxtamembrane domain to  
107 create a membrane-anchored C-terminal fragment ( $\beta$ -CTF) and a soluble extracellular APP  
108 domain (sAPP $\beta$ ).  $\beta$ CTF is further cleaved by the  $\gamma$ -secretase complex, which leads to the  
109 release of the  $A\beta$ -peptide. APP and its secretases co-localize in endosomal compartments  
110 where cleavage can occur (Wang et al., 2018). It has further been reported that BACE1 activity  
111 is preferentially active in acidic environments (Shimizu et al., 2008). We therefore investigated  
112 whether NHE6-depletion alters BACE1 activity in neurons and whether NHE6-deficiency leads  
113 to changes in plaque deposition *in vivo*. We found that NHE6 inhibition or knockdown did not  
114 alter BACE1 activity, as judged by unchanged  $A\beta$  generation. By contrast, NHE6 ablation led to  
115 glial activation and decreased plaque load in *ApoE*<sup>APOE4</sup> (Sullivan et al., 1997) and *App*<sup>NL-F</sup> (Saito  
116 et al., 2014) double knockin mice.

117

118

## 119 RESULTS

### 120 NHE6 is Required for Postnatal Purkinje Cell Survival

121 NHE6 germline knockout mice (*Slc9a6*<sup>-</sup>) and tamoxifen-inducible conditional NHE6  
122 knockout mice (*Slc9a6*<sup>fl</sup>;*CAG-Cre*<sup>ERT2</sup>) were generated as described in Materials and Methods  
123 and **Figure 2A-C**. To validate early endosomal pH acidification by NHE6-deficiency we isolated  
124 mouse embryonic fibroblasts from the *Slc9a6*<sup>-</sup> line and infected them with a Vamp3-pHluorin2  
125 lentivirus expressing a fusion protein consisting of the endosomal Vamp3 protein and the  
126 ratiometric pH indicator pHluorin2 (Stawicki et al., 2014). We found a significantly reduced  
127 number of vesicles with pH 6.4 and above in *Slc9a6*<sup>-</sup> fibroblasts when compared to control  
128 (**Figure 2D-F**).

129 To induce the conditional KO of *Slc9a6*, tamoxifen was administered to *Slc9a6*<sup>fl</sup>;*CAG-*  
130 *Cre*<sup>ERT2</sup> mice at two months (**Figure 3A**) and experiments were performed at the indicated time

131 points. *Slc9a6* knockout efficiency in the brains of tamoxifen injected *Slc9a6<sup>fl</sup>;CAG-Cre<sup>ERT2</sup>* mice  
132 was 65-82% and varied between brain regions (**Figure 3B**). To further investigate *Cre<sup>ERT2</sup>*  
133 activity upon tamoxifen-injection, we bred the *CAG-Cre<sup>ERT2</sup>* line with a stop-tdTomato reporter  
134 line in which a floxed stop-codon precedes the tdTomato start-codon. After tamoxifen injection,  
135 brains were examined for tdTomato expression. Without tamoxifen injection, tdTomato  
136 expressing cells were almost absent in the hippocampus. Tamoxifen induced recombination led  
137 to a broad expression of tdTomato in the hippocampus (**Figure 2G**).

138 Individuals with Christianson Syndrome and mice lacking NHE6 present with motor  
139 deficits due to a dramatic progressive loss of cerebellar Purkinje cells (Ouyang et al., 2013). We  
140 have reproduced the Purkinje cell loss in our germline *Slc9a6<sup>-/-</sup>* mice (**Figure 3C**). Next, we  
141 investigated whether Purkinje cell loss is the consequence of neurodevelopmental or  
142 neurodegenerative effects caused by loss of NHE6. *Slc9a6*-deficiency was induced at 2 months,  
143 after Purkinje cells had developed and matured. One year after *Slc9a6*-ablation Purkinje cell  
144 loss was indistinguishable from that seen in the germline knockouts (**Figure 3D-F**). Therefore,  
145 Purkinje cell degeneration manifests itself postnatally and is not developmentally determined by  
146 the absence of NHE6. However, it is possible that loss of scaffolding functions and proper  
147 sorting, rather than dysregulation of endosomal pH, could be the main mechanism that causes  
148 Christianson syndrome, including Purkinje cell loss (Ilie et al., 2020; Ilie et al., 2019). If this  
149 could be substantiated by the development or discovery of *Slc9a6* mutants that selectively  
150 ablate its ion exchange capacity without affecting its subcellular sorting or interaction with  
151 cytoplasmic or luminal binding partners, this would further raise the potential of NHE6 as a novel  
152 drug target for neurodegenerative diseases.

153

#### 154 **Genetic Disruption of NHE6 Restores Trafficking of Apoer2, AMPA and NMDA Receptors** 155 **in the Presence of ApoE4**

156 As we reported previously, ApoE4 impairs the trafficking of synaptic surface receptors  
157 (Chen et al., 2010). To monitor receptor recycling in neurons we made use of an assay where  
158 Reelin is used to modulate receptor surface expression. Reelin is applied to primary neurons for  
159 30 minutes in the presence or absence of naturally secreted, receptor binding-competent ApoE  
160 (**Figure 4**). Subsequently, surface biotinylation is performed and cells are harvested for

161 immunoblotting to quantify the amount of Apoer2 and glutamate receptors expressed on the  
162 neuronal surface (Chen et al., 2010; Xian et al., 2018).

163 We have shown previously that in the presence of ApoE4, Apoer2 and glutamate  
164 receptors recycle poorly to the neuronal surface. This recycling block could be resolved by  
165 endosomal acidification induced by shRNA knockdown of *Slc9a6* or by applying the NHE  
166 inhibitor EMD87580 (Xian et al., 2018). To further exclude a nonspecific effect caused by the  
167 inhibition of other NHE family members or by shRNA off-target effects, we applied this assay on  
168 neurons isolated from *Slc9a6*<sup>-</sup> embryos (**Figure 4B**). Apoer2 recycling was completely restored  
169 in *Slc9a6*<sup>-</sup> neurons treated with ApoE4 (**Figure 4C**). We previously reported that the addition of  
170 ApoE3 to neurons also affects Apoer2 trafficking to a small, but reproducible extent. This was  
171 also abolished in *Slc9a6*<sup>-</sup> neurons (**Figure 4C**). In addition, genetic loss of NHE6 equally  
172 restored the ApoE4-impaired surface expression of AMPA and NMDA receptor subunits (**Figure**  
173 **4D-F**).

174

#### 175 **Conditional Disruption of NHE6 Relieves Synaptic Reelin Resistance in *ApoE*<sup>APOE4</sup> mice**

176 Reelin can enhance long term potentiation (LTP) in hippocampal field recordings of  
177 *ApoE*<sup>APOE3</sup> but not *ApoE*<sup>APOE4</sup> acute brain slices (Chen et al., 2010). We previously showed that  
178 this Reelin-resistance in *ApoE*<sup>APOE4</sup> slices was attenuated by pharmacological NHE inhibition  
179 (Xian et al., 2018). To investigate if endogenous loss of NHE6 also restores synaptic plasticity in  
180 the presence of ApoE4 we performed hippocampal field recordings on *Slc9a6*<sup>fl</sup>;CAG-Cre<sup>ERT2</sup>  
181 mice bred to *ApoE*<sup>APOE3</sup> or *ApoE*<sup>APOE4</sup> mice. To avoid potentially compounding effects of NHE6  
182 deficiency during embryonic development (Ouyang et al., 2013), NHE6/*Slc9a6* gene disruption  
183 was induced at 8 weeks by intraperitoneal tamoxifen injection (Lane-Donovan et al., 2015).  
184 Electrophysiology was performed 3-4 weeks after NHE6-depletion in 3 months old mice  
185 (*Slc9a6*<sup>fl</sup>;CAG-Cre<sup>ERT2</sup>, **Figure 5B, 5D, 5F, and 5H**). Tamoxifen-injected *Slc9a6*<sup>fl</sup>;CAG-Cre<sup>ERT2</sup>-  
186 negative mice expressing human ApoE3 or ApoE4 served as controls (*ApoE*<sup>APOE3</sup> and  
187 *ApoE*<sup>APOE4</sup>, **Figure 5A, 5C, 5E, and 5G**). For field recordings hippocampal slices were perfused  
188 with Reelin as described (Beffert et al., 2005; Chen et al., 2010; Durakoglugil et al., 2009;  
189 Weeber et al., 2002). Conditional genetic loss of NHE6 resulted in a moderate reduction of the  
190 ability of Reelin to enhance LTP in *ApoE*<sup>APOE3</sup> mice (comparing **Figure 5A and 5E to 5B and**

191 **5F)**. By contrast, as reported previously (Chen et al., 2010), hippocampal slices from *ApoE*<sup>APOE4</sup>  
192 mice were completely resistant to LTP enhancement by Reelin (**Figure 5C and 5G**). This  
193 resistance was abolished when NHE6 was genetically disrupted in *ApoE*<sup>APOE4</sup> mice: Reelin  
194 application enhanced LTP (**Figure 5D and 5H**) in *ApoE*<sup>APOE4</sup>;*Slc9a6*<sup>fl</sup>;*CAG-Cre*<sup>ERT2</sup> to a  
195 comparable extent as in the *ApoE*<sup>APOE3</sup>;*Slc9a6*<sup>fl</sup>;*CAG-Cre*<sup>ERT2</sup> mice (**Figure 5B**). Synaptic  
196 transmission was monitored and input-output curves were generated by plotting the fiber volley  
197 amplitude, measured at increasing stimulus intensities, against the fEPSP slope. No significant  
198 differences were found (**Figure 5I and 5J**).

199

### 200 **NHE Inhibition or NHE6 Knockdown does not Alter $\beta$ -CTF Generation *in vitro***

201 Cleavage of APP by  $\gamma$ -secretase and the  $\beta$ -site APP cleaving enzyme 1 (BACE1)  
202 generates the short neurotoxic polypeptide A $\beta$ . Cleavage by BACE1 results in a membrane  
203 anchored fragment called  $\beta$ CTF, which is further processed by  $\gamma$ -secretase to yield the soluble  
204 A $\beta$  peptide. BACE1 processing of APP occurs in the Golgi complex, on the cell membrane, and  
205 after endocytosis in endosomes (Caporaso et al., 1994; Vassar et al., 1999). It has been  
206 reported that BACE1 activity increases with lower pH (Hook et al., 2002). In a recent *in vitro*  
207 study in a HEK293 cell line overexpressing APP and BACE1, NHE6 overexpression reportedly  
208 led to a reduction of A $\beta$  production and conversely shRNA knockdown of NHE6/*Slc9a6* resulted  
209 in an increase in A $\beta$  production (Prasad and Rao, 2015). To investigate if NHE6/*Slc9a6*  
210 deficiency contributes to APP processing by BACE1 in neurons, we used primary neurons  
211 derived from *AppSwe* (*Tg2576*) mice, an Alzheimer's disease mouse model that overexpresses  
212 human APP with the "Swedish" mutation (Hsiao et al., 1996). Neurons were treated with the  
213 NHE inhibitor EMD87580 or transduced with lentiviral shRNA directed against NHE6/*Slc9a6* in  
214 the presence or absence of the  $\gamma$ -secretase inhibitor L-685458.  $\beta$ CTF was detected using the  
215 monoclonal antibody 6E10 directed against A $\beta$ -residues 1-16 (**Figure 6**). Inhibition of  $\gamma$ -  
216 secretase in ApoE4-treated *AppSwe* neurons strongly enhanced  $\beta$ CTF accumulation, however,  
217 additional treatment with EMD87580 did not alter the amount of  $\beta$ CTF in the cell lysates (**Figure**  
218 **6A**). NHE6 knockdown using lentiviral shRNA also had no effect on the amount of  $\beta$ CTF (**Figure**  
219 **6B**). We conclude that NHE6 inhibition is unlikely to increase A $\beta$  production under near-  
220 physiological conditions.

221

## 222 **NHE6 Deficiency Reduces A $\beta$ Plaque Load in Human *App* Knockin Mice**

223 To further study the effect of NHE6-deficiency on A $\beta$  pathology *in vivo* we bred  
224 humanized *App*<sup>NL-F</sup> mice (Saito et al., 2014) to our germline NHE6 knockout line (*Slc9a6*<sup>-</sup>). In  
225 these *App*<sup>NL-F</sup> mice, the A $\beta$ -sequence has been completely humanized and the early onset AD  
226 Swedish mutation (5' located mutations encoding K670N and M671L = NL) and the  
227 Beyreuther/Iberian mutation (3' flanking mutation encoding I716F = F) were also introduced,  
228 resulting in increased A $\beta$  production, but physiological regulation of APP expression. This  
229 allowed us to determine the effect of A $\beta$  overproduction while keeping APP expression under  
230 the control of the endogenous promoter. *App*<sup>NL-F</sup>;*Slc9a6*<sup>-</sup> and control *App*<sup>NL-F</sup> littermates were  
231 aged to one year. Perfusion-fixed brains were harvested and analyzed by H&E staining,  
232 Thioflavin S staining to visualize plaque load, and A $\beta$ -immunohistochemistry. H&E staining did  
233 not reveal any obvious anatomical structural differences between genotypes, but brain size,  
234 cortical thickness, hippocampal area, and CA1 thickness were reduced, as described previously  
235 (Xu et al., 2017) (**Figure 7 – Figure Supplement 1**). Plaques were more frequent in *Slc9a6*  
236 *wild type* than *Slc9a6*<sup>-</sup> mice. To further investigate and quantify plaque load we analyzed the  
237 same brains after Thioflavin S staining (**Figure 7A**). We found an approximate 80% reduction of  
238 plaques in *Slc9a6*<sup>-</sup> mice when compared to littermate controls (**Figure 7B**).  
239 Immunohistochemistry against A $\beta$  showed the same reduction (**Figure 7 – Figure Supplement**  
240 **3A-B**). In addition, we analyzed soluble (TBS fraction) and insoluble (GuHCl and 70% FA  
241 fractions) A $\beta$  in cortical brain lysates of 1.5 year old *App*<sup>NL-F</sup>;*Slc9a6*<sup>-</sup> mice and their control  
242 littermates. The amount of insoluble A $\beta$  (GuHCl and 70% FA fractions) was reduced in NHE6-  
243 depleted mice by approximately 71%, when compared to their control littermates (**Figure 7 –**  
244 **Figure Supplement 3C-E**). The ~50% reduction in soluble A $\beta$  was statistically not significant in  
245 *Slc9a6*<sup>-</sup> lysates (TBS fraction).

246

## 247 **NHE6/*Slc9a6* Deficiency Reduces Plaque Load in *App*<sup>NL-F</sup>;*ApoE*<sup>APOE4</sup>**

248 To further investigate whether *Slc9a6*-deficiency also protects the brain from plaques in  
249 the presence of human ApoE4 instead of murine ApoE, we bred *Slc9a6*<sup>fl</sup>;*CAG-Cre*<sup>ERT2</sup>;  
250 *ApoE*<sup>APOE4</sup> with *App*<sup>NL-F</sup> mice. At two months of age we induced *Slc9a6*-ablation with tamoxifen

251 and aged the mice to 14 - 16 months. *Slc9a6*-deficiency on the background of human ApoE4  
252 reduced plaque deposition, as shown by Thioflavin S staining (**Figure 7 – Figure Supplement**  
253 **3F and 3G**) and 4G8 immunoreactivity (**Figure 7C and 7D**). The age-dependent increase in  
254 plaque load in *ApoE<sup>APOE4</sup>;App<sup>NL-F</sup>* mice was abolished or delayed when *Slc9a6* was depleted  
255 after 2 months of age (**Figure 8**). *App<sup>NL-F</sup>* mice expressing murine ApoE developed plaques at  
256 12 months (**Figure 7A and 7B**), compared to *ApoE<sup>APOE4</sup>;App<sup>NL-F</sup>* which showed a similar number  
257 of plaques at 15-16 months (**Figures 7C, 7D, 8, and Figure 7 – Figure Supplement 3F-G**).  
258 This delay of plaque deposition caused by the presence of human ApoE4 as opposed to murine  
259 ApoE is consistent with earlier findings by the Holtzman group (Liao et al., 2015). Importantly,  
260 NHE6/*Slc9a6* ablation induced at two months showed a comparable reduction of plaque load as  
261 germline NHE6/*Slc9a6* depletion. We conclude that plaque deposition is modulated by the  
262 presence of NHE6 postnatally and is not affected by NHE6 activity during development.

263

### 264 **NHE6/*Slc9a6* Deficiency Does Not Affect Cortical Thickness and Hippocampus Size in** 265 ***App<sup>NL-F</sup>;ApoE<sup>APOE4</sup>* cortices**

266 Xu et al. (2017) reported reduced cortex thickness and hippocampus volume in *Slc9a6*<sup>-/-</sup>  
267 mice, which we were able to reproduce in our germline *Slc9a6*<sup>-/-</sup> model (**Figure 7 – Figure**  
268 **Supplement 1**). In addition, based on their findings Xu et al. (2017) concluded that the  
269 difference in brain size was a combined result of both neurodevelopmental and  
270 neurodegenerative effects caused by NHE6/*Slc9a6* deficiency. Since both, germline deficiency  
271 and adult-onset deficiency of NHE6 causes massive Purkinje cell loss in the cerebellum (**Figure**  
272 **3C-E**), we next investigated the effect of conditional NHE6/*Slc9a6*-loss on hippocampal and  
273 cortical neuronal loss in our *App<sup>NL-F</sup>;ApoE<sup>APOE4</sup>* model (**Figure 7E-I**). We measured brain size,  
274 cortical thickness, hippocampal area, and CA1 thickness. In contrast to germline *Slc9a6*<sup>-/-</sup> mice  
275 (**Figure 7 – Figure Supplement 1**) none of the analyzed parameters differed significantly  
276 between *Slc9a6<sup>fl</sup>;CAG-Cre<sup>ERT2</sup>* and controls (**Figure 7E-I**), and we specifically did not detect any  
277 reduction in brain size compared to *Slc9a6<sup>fl</sup>;App<sup>NL-F</sup>;ApoE<sup>APOE4</sup>* littermate controls. This is  
278 consistent with the undergrowth model proposed by Xu et al. (2017) as we induced conditional  
279 disruption of NHE6/*Slc9a6* in the adult after postnatal brain growth was completed.

280

## 281 **NHE6 Deficiency Increases Iba1 and GFAP Expression in the Brain**

282 Neuroprotective astrocytes and microglia have been described to reduce A $\beta$  deposition in  
283 early stages of AD (Sarlus and Heneka, 2017). It has been reported that NHE6-deficiency leads  
284 to increased glial fibrillary acidic protein (GFAP) and ionized calcium-binding adapter molecule  
285 (Iba1) immunoreactivity in different brain regions (Xu et al., 2017). To validate if plaque load  
286 correlated with Iba1 and/or GFAP immunoreactivity, we performed DAB-immunostaining for  
287 both marker proteins. We found that Iba1 and GFAP immunoreactivity is increased in the white  
288 matter and to a lesser extent in the cortex of *App<sup>NL-F</sup>;Slc9a6<sup>-</sup>* (**Figure 9 – Figure Supplement**  
289 **1A, 1C, and 1D**) and *App<sup>NL-F</sup>;ApoE<sup>APOE4</sup>;Slc9a6<sup>fl</sup>;CAG-Cre<sup>ERT2</sup>* (**Figure 9 – Figure Supplement**  
290 **1B, 1E, and 1F**) mice compared to their littermate controls. There was a non-significant trend  
291 towards increased immunoreactivity for both markers in the hippocampus of the *Slc9a6<sup>-</sup>* group.  
292 Taken together, these data are consistent with the findings of the Morrow group in germline  
293 *Slc9a6<sup>-</sup>* mice (Xu et al., 2017). Neurodegeneration can be a trigger for glial activation (Yanuck,  
294 2019). However, our data on glial activation and cerebral volume in cKO mice, where  
295 NHE6/*Slc9a6* was disrupted postnatally, suggest that neurodegeneration induced by  
296 NHE6/*Slc9a6*-deficiency is unlikely to be the trigger for the glial activation we observe.

297

## 298 **Microglia and Astrocytes Surround Plaques in Both, *Slc9a6<sup>-</sup>* and Control *App<sup>NL-F</sup>* mice**

299 Conditional and germline *Slc9a6*-deficient *App<sup>NL-F</sup>* mice have a reduced number of  
300 plaques in the brain and an increase of Iba1 and GFAP labeled glia. Others have shown that A $\beta$   
301 plaques levels are reduced with increased plaque-associated microglia detected with a co-stain  
302 for Iba1 and A $\beta$  (Parhizkar et al., 2019; Zhong et al., 2019). In order to investigate the  
303 contribution of microglia and astrocytes to the observed plaque reduction we analyzed brain  
304 slices by costaining for A $\beta$  using the 6E10 antibody (**Figure 9 and Figure 9 – Figure**  
305 **Supplement 2**). Whereas the total amount of plaques labeled by 6E10 was reduced in *Slc9a6<sup>-</sup>*  
306 as compared to control mice (**Figure 9C**), the amount of microglia and astrocytes surrounding  
307 plaques did not differ between genotypes (**Figure 9D and G**). In addition, there was no  
308 difference between genotypes in the amount of microglia co-labeled with 6E10 (**Figure 9E**) or  
309 the intensity of immunoreactivity for 6E10 within microglia (**Figure 9F**).

310

## 311 DISCUSSION

312 The prevalence of Alzheimer's disease (AD) is increasing with life-expectancy in all  
313 human populations. ApoE4 is the most important genetic risk factor. This makes it of paramount  
314 importance to understand the underlying mechanisms by which ApoE4 contributes to the  
315 pathology of the disease in order to devise effective targeted therapies that can be deployed on  
316 a global scale. Only small molecule drug therapies or, alternatively, immunization approaches,  
317 can satisfy this requirement. Biologics, including monoclonal antibodies and potential viral gene  
318 therapy approaches, are unlikely to be sufficiently scalable. We have previously reported a  
319 novel small molecule intervention that has the potential to neutralize ApoE4 risk (Xian et al.,  
320 2018) through prevention of the ApoE4-induced endosomal trafficking delay of synaptic  
321 receptors by the early endosomal sorting machinery. The mechanistic basis of this conceptually  
322 novel intervention is the acidification of the early endosomal compartment through inhibition of  
323 NHE6. Remarkably and unexpectedly, loss of NHE6/*Slc9a6* effectively reduced A $\beta$   
324 accumulation even in the absence of ApoE4, suggesting that hyperacidification of early  
325 endosomes prevents amyloid plaque formation independently of ApoE4. NHE6/*Slc9a6*  
326 suppression or inhibition may thus be a universal approach to prevent amyloid buildup in the  
327 brain, irrespective of ApoE genotype. Our previous (Xian et al. 2018) and current studies thus  
328 suggest a novel mechanism to prevent ApoE4-risk for Alzheimer's disease and delay plaque  
329 formation. In addition, genome wide association studies (GWAS) in conjunction with studies on  
330 cell culture and mouse models of AD show that various AD risk factors enhance endo-lysosomal  
331 dysfunction (Knopman et al., 2021; Small et al., 2017; Verheijen and Sleegers, 2018), which  
332 potentially could be corrected by NHE6 inhibition.

333 Upon endocytosis, endosomes undergo gradual acidification controlled by vATPases  
334 which actively pump protons into the vesicular lumen, and by the Na<sup>+</sup>/H<sup>+</sup>-exchanger NHE6  
335 which functions as a regulatable proton leak channel. NHE6-depletion acidifies early and  
336 recycling endosomes (Lucien et al., 2017; Ohgaki et al., 2010; Ouyang et al., 2013; Xinhan et  
337 al., 2011). pH is an important regulator of the endolysosomal sorting machinery in which  
338 vesicles undergo multiple rounds of fusion. EEs undergo fusion and fission events in close  
339 proximity to the cell membrane. Recycling endosomes originate from EEs while they undergo  
340 early-to-late-endosomal maturation. In contrast to late endosomes, recycling endosomes do not

341 undergo further acidification (Jovic et al., 2010; Schmid, 2017). The pH of EEs and recycling  
342 endosomes is approximately 6.4-6.5 (Casey et al., 2010). This is normally sufficient to induce  
343 ligand receptor dissociation and enable cargo sorting. Our data, however, suggest that ApoE4  
344 dramatically delays this fast recycling step in neurons, where ApoE, Apoer2, and glutamate  
345 receptors co-traffic through fast recycling compartments upon Reelin stimulation (Xian et al.,  
346 2018). We have proposed that ApoE4 impairs vesicle recycling due to isoelectric precipitation  
347 and structural unfolding at the physiological pH of the EE environment. This delays the  
348 dissociation of ApoE4 from its receptors, which in turn prolongs the entry of ApoE4 - along with  
349 Apoer2 and glutamate receptors in the same vesicle - into the recycling pathway (illustrated in  
350 **Figure 1**). We conclude that ApoE4 net-charge affects its endosomal trafficking. This is further  
351 supported by recent findings by Arboleda-Velasquez and colleagues (Arboleda-Velasquez et al.,  
352 2019), who reported the presence of the “Christchurch” R136S mutation in an E3/E3 PS1  
353 mutation carrier without dementia. By neutralizing the positive charge of Arg136 in ApoE3, the  
354 IEP of this ApoE3 isoform is predicted to match that of ApoE2, which is protective against AD  
355 (Corder et al., 1994). ApoE2 homozygous carriers have an exceptionally low likelihood of  
356 developing AD (Reiman et al., 2020). Moreover, the Christchurch mutation is located within the  
357 heparin binding domain of ApoE, which reduces its affinity for cell surface heparan sulfate  
358 proteoglycans. That in turn would result in decreased uptake and thus depletion of ApoE in EEs.  
359 The net effect would be unimpeded trafficking of EE vesicles through the fast recycling  
360 compartment.

361 In dendritic spines, NHE6 co-localizes with markers of early and recycling endosomes  
362 and with the glutamate receptor subunit GluA1. In the hippocampus, NHE6 is highly expressed  
363 in the pyramidal cells of the CA and the granule cells of the dentate gyrus (Stromme et al.,  
364 2011). Apoer2 is present at the postsynaptic density of CA1 neurons (Beffert et al., 2005).  
365 During LTP induction, translocation of NHE6-containing vesicles to dendritic spine heads is  
366 enhanced (Deane et al., 2013) and glutamate receptors are recruited to the synaptic surface  
367 through fast recycling (Fernandez-Monreal et al., 2016). Our findings are consistent with a  
368 model where NHE6 serves as a pH-regulator of Reelin-controlled fast recycling endosomes  
369 containing Apoer2 and glutamate receptors. This mechanism possibly translates to other cell  
370 types and other ApoE receptors.

371 We previously showed that ApoE4 impairs Reelin-mediated receptor recruitment to the  
372 neuronal surface and this can be reversed by functionally disabling NHE6 in primary neurons,  
373 which results in the increased acidification of EEs to a level sufficiently different from the IEP of  
374 ApoE4, which then allows its efficient dissociation from its receptors. Conditional *Slc9a6* deletion  
375 accordingly alleviates the ApoE4-mediated resistance to Reelin-enhanced synaptic plasticity in  
376 hippocampal field recordings. (Gao et al., 2019; Xian et al., 2018)

377 Amyloid- $\beta$  ( $A\beta$ ) and tau, forming amyloid plaques and neurofibrillary tangles, are the  
378 defining features of AD pathology. As of today, it remains controversial how ApoE-isoforms  
379 interfere with  $A\beta$  and tau pathology. ApoE, which is primarily expressed by astrocytes, is the  
380 major lipid transporter in the brain and in an isoform-dependent manner affects inflammatory,  
381 endolysosomal and lipid-metabolic pathways (Gao et al., 2018; Minett et al., 2016; Van Acker et  
382 al., 2019; Xian et al., 2018). Most risk factors identified by genome-wide association studies,  
383 including but not limited to APOE, ABCA7, CLU, BIN1, TREM2, SORL1, PICALM, CR1 are  
384 members of one or more of these pathways (Kunkle et al., 2019). In recent years, endosomal  
385 dysfunction has increasingly gained acceptance as a causal mechanism for late-onset AD. Our  
386 findings now provide a mechanistic explanation how ApoE4 impairs endolysosomal trafficking  
387 and recycling, by interfering with vesicular sorting and maturation at a crucial bottleneck juncture  
388 of the endosomal trafficking machinery. This has far-reaching consequences for neuronal  
389 function, synaptic plasticity, and tau phosphorylation (Brich et al., 2003; Cataldo et al., 2000;  
390 Chen et al., 2005; Chen et al., 2010; Nuriel et al., 2017; Pensalfini et al., 2020). More  
391 specifically, ApoE4 causes abnormalities of Rab5-positive endosomes (Nuriel et al., 2017).  
392 Intriguingly, over-activation of the small guanosine triphosphatase (GTPase) Rab5, recapitulates  
393 neurodegenerative features of AD (Pensalfini et al., 2020).

394 ApoE4 alters APP processing and  $A\beta$ -degradation, (reviewed in (Benilova et al., 2012;  
395 Haass et al., 2012; Huynh et al., 2017; Lane-Donovan and Herz, 2017; Pohlkamp et al., 2017;  
396 Yamazaki et al., 2019)) and the ability of Reelin to protect the synapse from  $A\beta$  toxicity is  
397 impaired by ApoE4 (Durakoglugil et al., 2009).  $A\beta$ -oligomerization followed by plaque formation  
398 is one hallmark of AD. NHE6 controls endosomal pH, which can affect BACE1 activity, one of  
399 the two enzymes required to process APP to release the  $A\beta$ -peptide. Prasad and Rao (2015)  
400 reported that overexpression of NHE6 and full length APP in HEK293 cells, rather than its  
401 inhibition or knockdown, reduced  $A\beta$  generation, which conflicts with our findings in primary

402 cortical neurons (**Figure 6**). Although the cause of this discrepancy remains currently  
403 unresolved, it is possible that it is the result of the two fundamentally different experimental  
404 systems that were used in the respective studies, i.e. overexpression in immortalized kidney  
405 cells on one hand and primary cortical neuronal cultures on the other. Using a humanized  
406 *App*<sup>NL-F</sup> knockin mouse model we show that NHE6/*Slc9a6*-deficiency in one-year old animals  
407 reduces plaque deposition by approximately 80%. In *App*<sup>NL-F</sup> mice plaques can be identified as  
408 early as 9 months of age. Whereas plaque deposition only increases by less than twofold  
409 between 9 and 12 months of age, it increases tenfold between 12 and 18 months (Saito et al.,  
410 2014). Importantly, the reduction in plaque deposition by *Slc9a6*-deficiency persists from early  
411 (12 months) to later stages (18 months) of AD, as *Slc9a6*-deficient *App*<sup>NL-F</sup> animals aged 18  
412 months had a reduction in insoluble A $\beta$  by approximately 71%. NHE6/*Slc9a6* depletion in *App*<sup>NL-F</sup>  
413 *F*; *ApoE*<sup>APOE4</sup> mice showed a comparable reduction in plaque load (**Figure 7 and Figure 7 –**  
414 **Figure Supplement 3**). Our data are consistent with previous findings by the Holtzman group  
415 (Fagan et al., 2002) that showed that mouse ApoE promotes plaque deposition more potently  
416 than human ApoE4.

417 Prevention of plaque formation in our *Slc9a6* deficient model was likely caused by  
418 increased microglial activation and plaque phagocytosis (**Figure 7, Figure 7 – Figure**  
419 **Supplement 3, Figure 8, Figure 9, Figure 9 – Figure Supplement 1 and Figure 9 – Figure**  
420 **Supplement 2**). In the brains of AD patients and APP overexpressing mice, plaques are  
421 surrounded by reactive microglia and astrocytes (Meyer-Luehmann et al., 2008; Serrano-Pozo  
422 et al., 2013), but the pathological significance of this is incompletely understood. Beneficial or  
423 detrimental roles of reactive microglia and astrocytes in the degradation of A $\beta$  have been  
424 reported, depending on the activation state of these cells (Meyer-Luehmann et al., 2008;  
425 Ziegler-Waldkirch and Meyer-Luehmann, 2018). We observed an increase in reactive microglia  
426 and astrocytes resulting from NHE6/*Slc9a6*-depletion, which correlated with reduced plaque  
427 deposition in *App*<sup>NL-F</sup> mice, irrespective of the presence of either murine ApoE or human ApoE4.  
428 As murine ApoE exacerbates plaque deposition even more than ApoE4, the comparable plaque  
429 reduction in *Slc9a6*-deficient mice with murine *ApoE* or *ApoE*<sup>APOE4</sup> might be the result of a  
430 maximally accelerated early endosomal maturation and cargo transport in the absence of NHE6.  
431 When compared to control *App*<sup>NL-F</sup> mice, *Slc9a6*-deficient *App*<sup>NL-F</sup> mice show an increase in Iba1  
432 (microglia) and GFAP (astrocytes) immunoreactivity, but reduced A $\beta$  immunoreactivity.

433 Surprisingly, the intensity of GFAP and Iba1 in plaque areas was comparable between the  
434 groups. Moreover, even though A $\beta$  is reduced and Iba1 is increased in the *Slc9a6*<sup>-</sup>, the  
435 proportion of microglial structures containing A $\beta$  (6E10 antibody) was comparable between  
436 *Slc9a6*-deficient and control *App*<sup>NL-F</sup> mice, as was the intensity signal for 6E10. This suggests  
437 that microglia in the *Slc9a6*<sup>-</sup> may be more efficient in taking up and degrading A $\beta$ . Whether the  
438 reduction in plaques is due to the presence of an increased number of microglia and astrocytes  
439 that actively phagocytose nascent plaques, or whether endosomal acidification in microglia and  
440 astrocytes improves their ability to degrade or export A $\beta$  from the brain remains to be  
441 determined. It is tempting to speculate that the mechanism that leads to reduced plaque load in  
442 *Slc9a6*-deficient *App*<sup>NL-F</sup> mice may involve an increased catabolic rate (Shi et al., 2021), brought  
443 about by the accelerated acidification and vesicular trafficking of early endosomes.

444 It is also possible that *Slc9a6*-deficiency alters the efficiency of astrocytes to lipidate  
445 ApoE. In a mouse model, improved ApoE lipidation by the overexpression of ATP-binding  
446 cassette transporter family member A1 (ABCA1) decreased plaque deposition (Wahrle et al.,  
447 2005; Wahrle et al., 2008; Wahrle et al., 2004). During HDL assembly, ABCA1 shuttles between  
448 EE and the plasma membrane, a process also referred to as retroendocytosis (Ouimet et al.,  
449 2019). Moreover, membrane trafficking of ABCA1 is altered by ApoE in an isoform dependent  
450 fashion (Rawat et al., 2019). The *App*<sup>NL-F</sup> mouse model used in our study develops plaques at  
451 12 months (Saito et al., 2014) in the presence of murine ApoE. However, onset of plaque  
452 deposition in human *ApoE*<sup>APOE4</sup> mice was delayed by approximately three months. The effect of  
453 germline *Slc9a6*-deficiency and conditional *Slc9a6*-deficiency induced at two months had a  
454 comparable effect on plaque reduction in *App*<sup>NL-F</sup> and *App*<sup>NL-F</sup>;*ApoE*<sup>APOE4</sup> mice.

455 *Slc9a6*<sup>-</sup> and *Slc9a6*<sup>fl</sup>;*CAG-Cre*<sup>ERT2</sup> both show progressive Purkinje cell loss in the  
456 cerebellum, indicating that NHE6 requirement is cell-autonomous and not developmentally  
457 determined. *Slc9a6*<sup>-</sup> and *Slc9a6*<sup>fl</sup>;*CAG-Cre*<sup>ERT2</sup> show a comparable increase in immunoreactivity  
458 against Iba1 and GFAP. Increased glia reactivity can be a direct cell-autonomous effect of  
459 NHE6-loss or an indirect effect caused by NHE6-deficiency related neurodegeneration. As  
460 germline *Slc9a6*<sup>-</sup> mice present with a reduction in cortical thickness and hippocampal volume  
461 caused by both neurodevelopmental and neurodegenerative effects (Xu et al., 2017) (**Figure 7**  
462 **– Figure Supplement 1**), it is possible that neurodegeneration gives rise to glia activation.  
463 However, the tamoxifen induced *Slc9a6*<sup>fl</sup>;*CAG-Cre*<sup>ERT2</sup> mice do not present with a reduction in

464 cortical or hippocampal volume (**Figure 7**), yet have comparable immunoreactivity for markers  
465 of glial activation. Our study supports a temporally distinct function of NHE6 in the adult brain  
466 where the cerebrum requires NHE6 for development, but not for postnatal neuronal survival,  
467 whereas Purkinje cells in the cerebellum do. A similar dual function for NHE6 has been  
468 described previously by Xu et al. (2017). Moreover, this further indicates that reduced plaque  
469 load is also not an effect of neuronal loss. Therefore, our two mouse models together suggest  
470 that the observed increased glial activation is not caused by neuronal cell loss, but rather is  
471 likely a direct cell-autonomous effect of NHE6 loss of function. It thus remains to be determined  
472 whether endosomal acidification in NHE6 deficient microglia alone is sufficient to induce A $\beta$   
473 degradation and plaque reduction.

474 NHE6 is ubiquitously expressed in all cells of the body, however, in the CNS it is highly  
475 expressed in neurons where abundant synaptic vesicles and neurotransmitter receptors recycle  
476 in synapses (Lee et al., 2021a; Lee et al., 2021b) and to a lesser extent in glial cells (Zhang et  
477 al., 2014). Neuronal NHE6 plays a direct role in both synaptic development and plasticity,  
478 potentially through BDNF/TrkB (Deane et al., 2013; Ouyang et al., 2013) and other pathways.  
479 The impact of NHE6 loss in microglia and astrocytes is still unknown. Global *Slc9a6*-deficiency  
480 causes glial activation *in vivo*, which could be mediated through either a primary cell-  
481 autonomous mechanism or a secondary mechanism induced by damaged neurons. In ApoE4-  
482 expressing astrocytes, others have shown that overexpression of NHE6 increases LRP1 on the  
483 surface, which correlated with an increase in A $\beta$  uptake (Prasad and Rao, 2018). Microglia are  
484 the primary glial cells that degrade A $\beta$ ; thus, it will be imperative to determine how NHE6 levels  
485 alter A $\beta$  degradation selectively in astrocytes and microglia, respectively.

486 Early endosomal pH balance in phagocytic cells plays an important role in viral and  
487 bacterial infection response. In phagocytic cells, the deacidification of endosomes using  
488 pharmacological inhibitors like chloroquine has been shown to reduce endosomal toll like  
489 receptor (TLR) response (de Bouteiller et al., 2005; Fox, 1996; Kuznik et al., 2011; Wozniacka  
490 et al., 2006; Yang et al., 2016), suggesting that NHE6 depletion in microglia might conversely  
491 augment TLR response.

492 It would also be intriguing to test whether *Slc9a6*-deficiency increases cognitive  
493 performance in AD mouse models. In the current study we used *App*<sup>NL-F</sup> and *App*<sup>NL-F</sup>;*ApoE*<sup>APOE4</sup>  
494 mice as the most physiological currently available mouse models of AD that do not rely on

495 excessive amyloid overproduction. These mice, however, do not show cognitive impairments in  
496 spatial learning tests like Morris water maze (Saito et al., 2014) (own unpublished observations).  
497 Other neurobehavioral phenotypes have been described for *Slc9a6*<sup>-/-</sup> mice, which also  
498 recapitulate symptoms in Christianson syndrome patients, for example hyposensitivity to pain  
499 (Petitjean et al., 2020). Future studies on our novel tamoxifen inducible *Slc9a6*<sup>fl</sup>;*CAG-Cre*<sup>ERT2</sup>  
500 line will help to understand whether these symptoms are based on neurodevelopmental deficits  
501 caused by germline *Slc9a6*-deficiency or whether they can be reproduced by induced loss of  
502 NHE6 postnatally.

503 In conclusion, we have shown that both, the endosomal trafficking defect induced by  
504 ApoE4 in neurons as well as increased plaque deposition irrespective of ApoE genotype can be  
505 corrected by inhibition or genetic deletion of NHE6/*Slc9a6*, a key regulator of early endosomal  
506 pH. Accelerated acidification of early endosomes abolishes the ApoE4-induced Reelin  
507 resistance and restores normal synaptic plasticity in ApoE4 targeted replacement mice. The first  
508 FDA approved drug for AD treatment in 18 years is aducanumab (Sevigny et al., 2016), an  
509 antibody directed against A $\beta$ , which clears amyloid from the brain. However, amyloid removal in  
510 individuals already afflicted with AD provides at best marginal benefits at this stage. Moreover,  
511 in excess of 1 billion people world-wide are ApoE4 carriers, making early treatment with a  
512 complex biologic such as aducanumab impractical on the global scale. Here we have presented  
513 a potential alternative approach which should be adaptable to large-scale prevention treatment  
514 using blood-brain-barrier penetrant NHE6-specific inhibitors. Taken together, our combined data  
515 suggest that endosomal acidification has considerable potential as a novel therapeutic approach  
516 for AD prevention and possibly also for the prevention of disease progression.

517

518

## 519 **MATERIALS AND METHODS**

### 520 ***Animals***

521 All animal procedures were performed according to the approved guidelines (Animal  
522 Welfare Assurance Number D16-00296) for Institutional Animal Care and Use Committee  
523 (IACUC) at the University of Texas Southwestern Medical Center at Dallas.

524 The mouse lines Rosa-stop-tdTomato *B6.Cg-Gt(ROSA)26Sor<sup>tm9(CAG-tdTomato)Hze/J</sup>*  
525 (Madisen et al., 2010) (JAX #007909) and CAG-Cre<sup>ERT2</sup> *B6.Cg-Tg(CAG-cre/Esr1)5Amc/J* mice  
526 (Hayashi and McMahon, 2002)(JAX #004682), were obtained from The Jackson Laboratories  
527 (Bar Harbor, ME). ApoE3 and ApoE4 targeted replacement mice (*ApoE<sup>APOE3</sup>*, *ApoE<sup>APOE4</sup>*)  
528 (Knouff et al., 1999; Sullivan et al., 1997) were kind gifts of Dr. Nobuyo Maeda. *AppSwe*  
529 (*Tg2576*) were generated by (Hsiao et al., 1996). The Meox-Cre *B6.129S4-Meox2tm1(cre)Sor/J*  
530 mice (JAX 003755) were provided by Drs. M. Tallquist and P. Soriano (Tallquist and Soriano,  
531 2000). Conditional NHE6 knockout (*Slc9a6<sup>fl</sup>;CAG-Cre<sup>ERT2</sup>*) and germline NHE6 knockout  
532 (*Slc9a6<sup>-/-</sup>*) mice were generated as described below. The human APP knockin line (*App<sup>NL-F</sup>*)  
533 (Saito et al., 2014) has been described earlier. Pregnant female SD (Sprague Dawley) rats were  
534 obtained from Charles River (SC:400). Mice were group-housed in a standard 12-h light/dark  
535 cycle and fed ad libitum standard mouse chow (Envigo, Teklad 2016 diet as standard and  
536 Teklad 2018 diet for breeding cages).

537 To generate *Slc9a6* floxed (*Slc9a6<sup>fl</sup>*) mice, the first exon of NHE6 was flanked with loxP  
538 sites (**Figure 2A**). A loxP site was inserted 2 kb upstream of the first exon of the X-chromosomal  
539 NHE6 gene and a Neo-cassette (flanked with loxP and FRT sites) was inserted 1 kb  
540 downstream of the first exon. Insertion sites were chosen based on low conservation (mVISTA)  
541 between mammalian species (rat, human, mouse). To create the targeting vector for the *Slc9a6<sup>fl</sup>*  
542 mouse line, pJB1 (Braybrooke et al., 2000) was used as backbone. Murine C57Bl/6J embryonic  
543 stem (ES) cell DNA was used as template to amplify the short arm of homology (SA; 0.88 kb of  
544 the first intron starting 1kb 3' downstream of exon 1), which was inserted between the Neo and  
545 HSVTK selection marker genes of pJB1 (BamHI and XhoI sites) to create an intermediate  
546 plasmid referred to as pJB1-NHE6SA. To create the intermediate plasmid pNHE6-LA for the  
547 long homology arm, a fragment spanning from 13kb 5' upstream to 1kb 3' downstream of the  
548 first *Slc9a6* (NHE6) exon was integrated into pCR4-TOPO (Thermo Fisher) by using a bacterial  
549 artificial chromosome (BAC, RP23 364F14, Children's Hospital Oakland Research Institute  
550 (CHORI)) and the GAP repair technique (Lee et al., 2001) (primers to amplify the upstream (US)  
551 and downstream (DS) homology boxes are listed in the Key Resources Table). In a parallel  
552 cloning step a 2.4 kb XhoI-EcoRV *Slc9a6*-promoter region fragment spanning from 2.7 kb to 0.4  
553 kb 5' upstream of the *Slc9a6* start codon was modified with the 1<sup>st</sup> loxP site to generate pLoxP:  
554 three fragments (1) 0.7 kb 5' loxP flanking *Slc9a6*-fragment, (2) 1.7 kb 3' loxP flanking *Slc9a6*-

555 fragment, and (3) 100 bp loxP oligo (primers/oligos for each fragment are listed in the Key  
556 Resources Table) were cloned into pCR4-TOPO. The 2.5 kb loxP-modified XhoI-EcoRV *Slc9a6*-  
557 promoter fragment of pLoxP was cloned into pNHE6-LA to create pNHE6-LA-LoxP. To obtain  
558 the final targeting construct pJB-NHE6-TV, the NotI-EagI fragment of pNHE6-LA-LoxP  
559 containing the long arm (11 kb 5' upstream of the 1<sup>st</sup> loxP) and the 1<sup>st</sup> loxP site was cloned into  
560 the NotI-site of pJB1-NHE6SA and checked for orientation (pJB1-NHE6 targeting vector). pJB-  
561 NHE6-TV was linearized with NotI and electroporated into C57Bl/6J ES cells. Gene targeting-  
562 positive C57Bl/6J ES cells (PCR-screen) were injected into albino C57Bl/6J blastocysts,  
563 resulting in chimeric mice. The chimeras were crossed to C57Bl/6J mice, resulting in *Slc9a6*<sup>fl/+</sup>  
564 females. Genotyping: The *Slc9a6*<sup>fl</sup> PCR amplifies a 250 bp of the wildtype and 270 bp of the  
565 floxed allele, primers are listed in the Key Resources Table.

566 To generate *Slc9a6*<sup>fl</sup>;*CAG-Cre*<sup>ERT2</sup>, *Slc9a6*<sup>fl/+</sup> females were crossed to *CAG-Cre*<sup>ERT2</sup> mice  
567 to obtain *Slc9a6*<sup>fl/fl</sup>;*CAG-Cre*<sup>ERT2</sup> and *Slc9a6*<sup>y/fl</sup>;*CAG-Cre*<sup>ERT2</sup> mice (*Slc9a6*<sup>fl</sup>;*CAG-Cre*<sup>ERT2</sup>) and  
568 *CAG-Cre*<sup>ERT2</sup> negative control littermates (*Slc9a6*<sup>fl</sup>). *Slc9a6*<sup>fl</sup>;*CAG-Cre*<sup>ERT2</sup> mice were  
569 backcrossed to *ApoE*<sup>APOE3</sup> or *ApoE*<sup>APOE4</sup> mice. Breeding pairs were set up in which only one  
570 parent was *CAG-Cre*<sup>ERT2</sup> positive. The following genotypes were used for hippocampal field  
571 recordings: (1) *ApoE*<sup>APOE3</sup>;*SLC9a6*<sup>y/fl</sup> (short:*ApoE*<sup>APOE3</sup>), (2) *ApoE*<sup>APOE3</sup>;*Slc9a6*<sup>y/fl</sup>;*Cre*<sup>ERT2</sup> (short:  
572 *ApoE*<sup>APOE3</sup>; *Slc9a6*<sup>fl</sup>;*CAG-Cre*<sup>ERT2</sup>), (3) *ApoE*<sup>APOE4</sup>;*Slc9a6*<sup>y/fl</sup> (short: *ApoE*<sup>APOE4</sup>), and (4)  
573 *ApoE*<sup>APOE4</sup>;*SLC9a6*<sup>y/fl</sup>;*Cre*<sup>ERT2</sup> (short: *ApoE*<sup>APOE4</sup> ;*Slc9a6*<sup>fl</sup>;*CAG-Cre*<sup>ERT2</sup>). The  
574 *ApoE*<sup>APOE4</sup>;*Slc9a6*<sup>fl</sup>;*CAG-Cre*<sup>ERT2</sup> line was further crossed with the *App*<sup>NL-F</sup> line to generate  
575 *ApoE*<sup>APOE4</sup>;*Slc9a6*<sup>fl</sup>;*CAG-Cre*<sup>ERT2</sup>;*App*<sup>NL-F</sup> and *ApoE*<sup>APOE4</sup>;*Slc9a6*<sup>fl</sup>;*App*<sup>NL-F</sup> control littermates. To  
576 induce genetic depletion of NHE6, tamoxifen (120 mg/kg) was intraperitoneally injected at 6-8  
577 weeks of age. Injections were applied for five consecutive days. Tamoxifen was dissolved in  
578 sunflower oil (Sigma, W530285) and 10% EtOH.

579 To generate the germline NHE6 knockout line (*Slc9a6*<sup>-</sup>), heterozygous *Slc9a6*<sup>fl/+</sup> females  
580 were crossed to *Meox-Cre* to yield germline mutant *Slc9a6*<sup>-/-</sup> females and *Slc9a6*<sup>y/-</sup> males  
581 (*Slc9a6*<sup>-</sup>). Genotyping: The *Slc9a6*<sup>fl</sup> PCR amplifies 250 bp of the wildtype, 270 bp of the floxed,  
582 and no fragment in the knockout alleles. Recombination was verified with the NHE6-rec PCR,  
583 which amplifies 400 bp if recombination has occurred. PCR-primers are listed in the Key  
584 Resources Table. *Slc9a6*<sup>-</sup> animals were further crossed with *App*<sup>NL-F</sup> (Saito et al., 2014) mice.  
585 *App*<sup>NL-F</sup>;*Slc9a6*<sup>-</sup> (*App*<sup>NL-F/NL-F</sup>;*Slc9a6*<sup>y/-</sup> or *App*<sup>NL-F/NL-F</sup>;*Slc9a6*<sup>-/-</sup>) and control (*App*<sup>NL-F</sup> = *App*<sup>NL-F/NL-F</sup>)

586  $F$ ;  $Slc9a6^{y/+}$  or  $App^{NL-F/NL-F}; Slc9a6^{+/+}$ ) littermates were obtained by crossing  $Slc9a6^{+/+}; App^{NL-F/NL-F}$   
587 females with either  $Slc9a6^{y/+}; App^{NL-F/NL-F}$  or  $Slc9a6^{y/-}; App^{NL-F/NL-F}$  males.

588

### 589 **DNA Constructs, Recombinant Proteins, Lentivirus Production**

590 Lentiviral plasmids with shRNA directed against NHE6/ $Slc9a6$  and the scrambled control  
591 have been described in Xian et al. (Xian et al., 2018). Plasmids encoding ApoE3 and ApoE4  
592 (Chen et al., 2010), and Reelin (D'Arcangelo et al., 1997) have been described before. The  
593 lentiviral plasmid encoding the Vamp3-pHluorin2 fusion protein was cloned by inserting mouse  
594 Vamp3 cDNA, a linker and pHluorin2 (pME, Addgene #73794) (Stawicki et al., 2014) into  
595 pLVCMVfull (Xian et al., 2018). For Vamp3 the forward primer (5'-  
596 TTCAAGCTTCACCATGTCTACAGGTGTGCCTTCGGGGTC-3') contains a Kozak sequence,  
597 the reverse primer encodes a KLSNSAVDGTAGPGSIAT-linker (Nakamura et al., 2005) (5'  
598 CATTGTCATCATCATCATCGTGTGGTGTGTCTCTAAGCTGAGCAACAGCGCCGTGGACGGC  
599 ACCGCCGGCCCCGGCAGCATCGCCACCAAGCTTAAC-3'). The pHluorin2 primers were  
600 forward 5'-CCGGTCCCAAGCTTATGGTGAGCAAGGGCGAGGAGCTGTTC-3' and reverse 5'-  
601 GCCCTTTCTAGAGAATTCACCTTGTACAGCTCGTCCATGCCGTG-3'. The fragments were  
602 sequentially cloned into pcDNA3.1 and the fusion protein was then transferred with NheI and  
603 EcoRI into pLVCMVfull. Lentiviral plasmids psPAX2 and pMD2.g were a kind gift from Dr D.  
604 Trono and obtained from Addgene.

605 Recombinant Reelin and ApoE were generated in 293HEK cells. Reelin was purified as  
606 described before (Weeber et al., 2002). ApoE-conditioned medium was collected from HEK293  
607 cell cultures transiently transfected with pcDNA3.1-ApoE constructs or empty control vector  
608 (pcDNA3.1-Zeo). ApoE concentration was measured as described before (Xian et al., 2018).

609 For lentivirus production HEK 293-T cells were co-transfected with psPAX2, pMD2.g, and  
610 the individual shRNA encoding transfer or Vamp3-pHluorin2 constructs. Media was replaced  
611 after 12-16 hours. Viral particle containing media was collected after centrifuging cellular debris.  
612 The viral particles were 10x concentrated by ultra-centrifugation and resuspended in Neurobasal  
613 medium. To infect neurons on DIV7 1/10<sup>th</sup> of the culture medium was replaced by concentrated  
614 virus. After 24 hours the virus was removed.

615

## 616 **Histochemistry**

617 Mice were euthanized with isoflurane and perfused with PBS followed by 4%  
618 paraformaldehyde (PFA) in PBS. Brains were removed and post-fixed for 24 hours in 4% PFA.  
619 Fresh fixed brains were immobilized in 5% agarose in PBS and 50  $\mu\text{m}$  thick sections were sliced  
620 on a vibratome (Leica, Wetzlar, Germany). Vibratome slices of Rosa26<sup>flox</sup>Stop-  
621 <sup>tdTomato</sup>;CAGCre<sup>ERT2</sup> mice, with or without tamoxifen injection at 8 weeks of age were mounted  
622 with Antifade Mounting medium containing DAPI (Vectashield). For immunofluorescence,  
623 vibratome slices were labeled for Calbindin after permeabilization with 0.3% Triton X in PBS and  
624 blocking for 1 hour in blocking buffer (10% normal goat serum, 3% BSA, and 0.3% Triton X in  
625 PBS). The primary antibody mouse anti-Calbindin (Swant CB300) was diluted in blocking buffer  
626 (1:1000) and added to the slices for 24-48 h at 4°C. Slices were subsequently washed 4x 15  
627 min with PBS containing 0.3% Triton X. Slices were incubated with anti-mouse IgG coupled to  
628 Alexa594 (1:500 in blocking buffer) for 2 hours at room temperature. After washing, slices were  
629 mounted with Antifade Mounting medium with DAPI (Vectashield). Images were taken with an  
630 Axioplan 2 microscope (Zeiss).

631 For immunohistochemistry staining, PFA fixed brains were block-sectioned into coronal  
632 slabs, paraffin-embedded, and serially sectioned on a rotating microtome (Leica) at 5  $\mu\text{m}$ .  
633 Deparaffinized sections were stained with Thioflavin S as described before (Guntern et al.,  
634 1992). Briefly, deparaffinized slices were oxidized in 0.25%  $\text{KMnO}_4$  for 20 min. After washing  
635 with water slices were bleached with 1%  $\text{K}_2\text{S}_2\text{O}_5$  /  $\text{C}_2\text{H}_2\text{O}_4$  for 2 min, washed in water, and  
636 treated with 2%  $\text{NaOH}/\text{H}_2\text{O}_2$  for 20 min. After washing with water slices were acidified in 0.25%  
637  $\text{CH}_3\text{COOH}$  for 1 min, washed with water and equilibrated in 50% EtOH for 2 min, and stained in  
638 Thioflavin S solution for 7 min. Reaction was stopped by washing in 50% EtOH. Slices were  
639 dehydrated with 95% EtOH, followed by 100% EtOH and Xylene. Slices were mounted with  
640 Cytoseal 60 (Thermo Scientific). Deparaffinized sections were labeled using antibodies raised  
641 against GFAP (Abcam AB5804, Rabbit, 1:2,000), Iba1 (Wako 019-19741, Rabbit, 1:1,000), and  
642 A $\beta$  (4G8, Covance or 6E10, Biolegend, both mouse, 1:1,000). Briefly, 5  $\mu\text{m}$  sections were  
643 deparaffinized, subjected to microwave antigen retrieval (citrate buffer, pH 6.0), permeabilized  
644 with 0.3% (vol/vol) Triton X, endogenous peroxidases activity was quenched for

645 Diaminobenzidine (DAB) staining. Slices were blocked with goat serum (2.5 %) prior to  
646 overnight incubation with primary antibodies at 4°C. Primary antibodies were detected by either  
647 fluorescent secondary antibodies (goat-anti-mouse Alexa594, goat-anti-rabbit Alexa488) or  
648 sequential incubation with biotinylated secondary antisera and streptavidin-peroxidase for DAB  
649 staining. Diaminobenzidine chromagen was used to detect the immunoperoxidase signal  
650 (Sinclair et al., 1981) (Vector; anti-mouse and anti-rabbit IgG kits). Fluorescence-labeled slices  
651 were counter-stained with DAPI (mounting media with DAPI, Vectashield). Standard protocols  
652 were utilized for staining of paraffin sections with hematoxylin and eosin (H&E; Leica) (Fischer  
653 et al., 2008). Microscopy was performed on a high-throughput microscope (NanoZoomer 2.0-  
654 HT, Hamamatsu) for DAB stained tissue or with an Axioplan 2 microscope (Zeiss) for  
655 immunofluorescence analysis. The analysis of DAB labeled antibodies was performed after  
656 exporting the images with NDP.view2 software with ImageJ. For Thioflavin S staining and A $\beta$   
657 labeling plaques were quantified by categorizing them as small, medium, and large (Thioflavin  
658 S) or dense and diffuse (4G8) as depicted in **Figure 7 – Figure Supplement 2**. Co-localization  
659 analysis of microglia (Iba1) and astrocytes (GFAP) with plaques (6E10) was performed with  
660 ImageJ. A blind observer selected the area of plaques with circles of 20, 40, or 80  $\mu$ m diameter  
661 and analyzed the intensity of 6E10 and Iba1 or GFAP by using the ImageJ plugin  
662 RGB\_measure. 6E10 positive microglia (Iba1) were quantified by a blind observer by first  
663 identifying microglia structures/cells in the green channel (Iba1), and then analyzing the  
664 proportion of 6E10 positive structures and signal intensity (red channel).

665

### 666 ***Primary Cortical Neuronal Cultures***

667 Primary cortical neuronal cultures were prepared from rat (SD, Charles River) or various  
668 mouse lines (*wildtype*, *Slc9a6*<sup>-</sup>, *AppSwe*) (E18) as described previously (Chen et al., 2005).  
669 Neurons were cultured in Poly-D-Lysine coated 6-well plates (1 million / 9 cm<sup>2</sup>) or on coverslips  
670 (30,000 neurons / 1.1 cm<sup>2</sup>) in presence of Neurobasal medium supplemented with B27,  
671 glutamine, and Penicillin-Streptomycin at 37°C and 5% CO<sub>2</sub>. At indicated days in vitro (DIV)  
672 primary neurons were used for experiments.

673

### 674 ***Mouse Embryonic Fibroblasts***

675 Fibroblasts were isolated from *Slc9a6*<sup>-</sup> and wildtype littermate control embryos (E13.5).  
676 After removing the head and the liver, the tissue was trypsinized (0.05% trypsin-EDTA) at 4°C  
677 overnight, followed by 30 min at 37°C. Suspended cells were cultivated in DMEM high glucose  
678 with 15% FCS, 2 mM L-glutamine, and Pen/Strep. Fibroblasts were serially passaged until  
679 proliferation slowed down. Immortalization was achieved by keeping fibroblasts in culture under  
680 high confluency until they overcame their growth-crisis.

681

## 682 ***pH Measurements***

683 Mouse embryonic fibroblasts derived from either *Slc9a6*<sup>-</sup> or wildtype littermate embryos  
684 were infected with Vamp3-pHluorin2 lentivirus. 24-48 hours post infection, vesicular pH was  
685 measured on a Zeiss LSM880 Airyscan confocal microscope as described in Ma et al. (Ma et  
686 al., 2017). For the standard calibration curve, cells were washed and incubated with pH  
687 standard curve buffer (125 mM KCl, 25 mM NaCl, 10 μM monensin, 25 mM HEPES for pH > 7.0  
688 or 25 mM MES for pH < 7.0; pH adjusted with NaOH and HCl) and imaged in 5% CO<sub>2</sub> at 37°C.  
689 For vesicular pH measurements, cells were washed and imaged with pH standard curve at pH 7  
690 without monensin. Samples were excited at 405 and 488 nm with an emission of 510 nm. For  
691 quantification, 6 fields of view were imaged for *Slc9a6*<sup>+</sup> and 4 fields of view for *Slc9a6*<sup>-</sup> fibroblast.  
692 Between 4-10 pHluorin-positive vesicles were measured per field of view which resulted in n=32  
693 wildtype vesicle and n=28 *Slc9a6*<sup>-</sup> vesicles. The same settings were used for every image, and  
694 images were analyzed using ImageJ Software. The intensity of excitations with 405 and 488 nm  
695 was measured, individual vesicles were marked as regions of interest, and the 405/488 ratio  
696 was calculated and plotted against pH for the standard curve.

697

## 698 ***Biochemistry***

699 To analyze receptor recycling cell surface biotinylation was performed. At DIV10-14,  
700 primary neurons were pre-treated for 30 min with ApoE-conditioned medium (5 μg/ml) and  
701 incubated with Reelin (2 μg/ml) for an additional 30 min (see timeline in **Figure 4A**). After  
702 treatment, cells were washed with cold PBS and incubated in PBS containing sulfo-NHS-SS-  
703 biotin for 30 min at 4°C. Subsequently excess reagent was quenched by rinsing the neurons

704 with cold PBS containing 100 mM glycine. Neurons were lysed in 160  $\mu$ l/ 9 cm<sup>2</sup> lysis buffer (PBS  
705 with 0.1% SDS, 1% Triton X-100, and protease inhibitors) at 4°C for 20 min. Cell debris were  
706 pelleted at 14,000 rpm for 10 min at 4°C. The protein concentration was measured using the  
707 Bradford Protein Assay (Bio-Rad). One hundred  $\mu$ g of total proteins were incubated with 50  $\mu$ l of  
708 NeutrAvidin agarose at 4°C for 1 hour. Agarose beads were washed three times using washing  
709 buffer (500 mM NaCl; 15 mM Tris-HCl, pH 8.0; 0.5% Triton X-100), biotinylated surface proteins  
710 were eluted from agarose beads by boiling in 2x SDS sample loading buffer and loaded on an  
711 SDS-PAGE gel for Western blot analysis. GST-control and GST-RAP (50  $\mu$ g/ml) pre-treatment  
712 of neurons was performed for 1 hour.

713 To analyze BACE1 activity,  $\beta$ CTF was detected by immune blotting. BACE1 activity was  
714 examined after pharmacological NHE inhibition or genetic *Slc9a6* knockdown in primary  
715 neurons of *AppSwe* mice. For NHE inhibition DIV10 neurons were treated with 5  $\mu$ g/ml ApoE4, 3  
716  $\mu$ M EMD87580 (Merck), and/or 1  $\mu$ M  $\gamma$ -secretase inhibitor L-685458 (Merck) for 5 hours. For  
717 knockdown of *NHE6/Slc9a6* DIV7 neurons of *AppSwe* mice were infected with lentivirus  
718 encoding shRNA against NHE6 or a scrambled control shRNA. On DIV13 neurons were treated  
719 with  $\gamma$ -secretase inhibitor for 12 hours. Proteins were extracted for Western blot analysis: Cells  
720 were washed three times with cold PBS, and lysed for 20 min on ice in RIPA buffer (50 mM Tris-  
721 HCl, pH 8.0; 150 mM NaCl; 1% Nonidet P-40; phosphatase and proteinase inhibitors). Cell  
722 debris were pelleted at 14,000 rpm for 10 min at 4°C. Protein concentration was measured  
723 using the Bradford Protein Assay (Bio-Rad). After adding 4xSDS loading buffer (0.1 M Tris-HCl,  
724 pH 6.8, 2% SDS, 5%  $\beta$ -mercaptoethanol, 10% glycerol, and 0.05% bromophenol blue) samples  
725 were denatured at 80°C for 10 min. Proteins were separated via SDS-PAGE and transferred to  
726 a nitrocellulose membrane for Western blotting using different antibodies listed in the Key  
727 Resources Table.

728 Brain tissue was dissected and prepared for immunoblotting as followed: After removal,  
729 brains were placed in ice-cold PBS containing proteinase inhibitors. Anatomical sectioning was  
730 performed under a microscope. The hippocampus was dissected out and transversal slices  
731 were further separated into Cornu Ammonis (CA) 1, CA3, and dentate gyrus. Respective pieces  
732 of the same anatomical regions of one brain were pooled, shock-frozen in liquid nitrogen and  
733 stored at -80C. Frozen tissue was homogenized in 10x volume of RIPA buffer and incubated on

734 ice for 30 min. Cell debris were pelleted for 10 min with 14,000 rpm at 4°C. After adding 4xSDS  
735 loading buffer the samples were denatured at 80°C for 10 min and used for immunoblotting.

736 To measure soluble and insoluble A $\beta$  species, a sequential homogenization procedure  
737 was employed. After removal of the brains from PBS perfused mice, cortical tissue was  
738 dissected and flash frozen. Frozen cortical tissue was homogenized in TBS supplemented with  
739 phosphatase and proteinase inhibitors at 100 mg protein/ml using a glass dounce homogenizer.  
740 Crude lysate was centrifuged at 800  $xg$  for 5 min at 4°C. The supernatant was further  
741 centrifuged at 100,000  $xg$  for 30 min at 4°C and collected as TBS-soluble lysate (A $\beta$ -soluble).  
742 The TBS-pellet was further homogenized in 1% Triton-TBS containing phosphatase and  
743 proteinase inhibitors, centrifuged at 100,000  $xg$  for 30 min at 4°C and collected as 1% Triton-  
744 soluble lysate. The Triton-pellet was incubated with 5M guanidine-HCl rotating at RT for 1 hour.  
745 Guanidine soluble lysate (A $\beta$ -insoluble) was collected after centrifugation at 21,000  $xg$  for 15  
746 min at 4°C. The guanidine-pellet was further solubilized in 1/20<sup>th</sup> volume with 70% Formic Acid  
747 (A $\beta$ -insoluble) and centrifuged at 21,000  $xg$  for 15 min at 4°C. Soluble and insoluble A $\beta$  levels  
748 were measured in duplicates using a commercial A $\beta$ 42 ELISA kit (ThermoFisher, KHB3441)  
749 following the manufacturer's instructions.

750

### 751 ***Extracellular Field Recordings***

752 Hippocampal slices were prepared from 3-month-old mice (tamoxifen-injected at 8  
753 weeks). Slices of mice were obtained from four different genotypes; *Slc9a6<sup>fl</sup>*; *CAG-Cre<sup>ERT2</sup>* mice  
754 or *Slc9a6<sup>fl</sup>* mice with *ApoE<sup>APOE3</sup>* or *ApoE<sup>APOE4</sup>*. The brains were quickly removed and placed in  
755 ice cold high sucrose cutting solution (in mM: 110 sucrose, 60 NaCl, 3 KCl, 1.25 NaH<sub>2</sub>PO<sub>4</sub>, 28  
756 NaHCO<sub>3</sub>, 0.5 CaCl<sub>2</sub>, 5 glucose, 0.6 Ascorbic acid, 7 MgSO<sub>4</sub>), bubbled with a gas mixture of 95%  
757 O<sub>2</sub> and 5% CO<sub>2</sub> for oxygenation. 350  $\mu$ m transverse sections were cut using a vibratome  
758 (Leica). Slices were transferred into an incubation chamber containing 50% artificial  
759 cerebrospinal fluid (aCSF, in mM: 124 NaCl, 3 KCl, 1.25 NaH<sub>2</sub>PO<sub>4</sub>, 26 NaHCO<sub>3</sub>, 10 D-glucose,  
760 2 CaCl<sub>2</sub>, 1 MgSO<sub>4</sub>) and 50% sucrose cutting solution, oxygenated with 95%O<sub>2</sub>/5%CO<sub>2</sub>. Slices  
761 were transferred into an oxygenated interface chamber and perfused with aCSF with or without  
762 Reelin (2  $\mu$ g/ml). The stimulating electrode was placed on the Schaffer-collateral of the CA1-  
763 pyramidal neurons and the recording electrode on the dendrites of the CA3-pyramidal neurons.

764 Once baseline was stably recorded for 20 min, theta burst was applied and traces collected for  
765 an hour. For stimulation concentric bipolar electrodes (FHC, catalog no CBBRC75) were placed  
766 into the stratum radiatum. Stimulus intensity was set at 40-60% of maximum response and  
767 delivered at 33 mHz through an Isolated Pulse Stimulator (A-M Systems, Model 2100). A  
768 custom written program in LabView 7.0 was used for recording and analysis of LTP  
769 experiments. A theta burst (TBS; train of 4 pulses at 100 Hz repeated 10 times with 200 ms  
770 intervals; repeated 5 times at 10 s intervals) was used as a conditioning stimulus.

771

## 772 ***Statistical Methods***

773 Data were expressed as the mean  $\pm$  SEM and evaluated using two-tailed Student's t-test  
774 for two groups with one variable tested and equal variances, one-way analysis of variance  
775 (ANOVA) with Dunnett's post-hoc or Tukey's post-hoc for multiple groups with only variable  
776 tested, or two-way ANOVA with Sidak's post-hoc for plaque quantification (two independent  
777 variables of NHE6 genotype and plaque classification). The differences were considered to be  
778 significant at  $p < 0.05$  (\* $p < 0.05$ , \*\*  $p < 0.01$ , \*\*\*  $p < 0.001$ ). Software used for data analysis was  
779 ImageJ (NIH), LabView7.0 (National Instruments), Odyssey Imaging Systems (Li-Cor), Prism7.0  
780 (GraphPad Software).

781

## 782 **ACKNOWLEDGEMENTS**

783 This work was supported by NIH grants R37 HL063762, R01 NS093382, R01 NS108115,  
784 and RF1 AG053391 to JH and 1F31 AG067708-01 to CHW as well as funding from the Darrell  
785 K. Royal Research Fund to MD. While this work was ongoing, JH was further supported by the  
786 Bright Focus Foundation (A20135245) & (A2016396S); Harrington Discovery Institute; & Circle  
787 of Friends Pilot Synergy Grant; and the Blue Field Project to Cure FTD. We are indebted  
788 Rebekah Hewitt, Barsha Subbha, Huichuan Reyna, Issac Rocha, Tamara Terrones, Emily  
789 Boyle, Alisa Gilloon, Travis Wolff, and Eric Hall for their excellent technical assistance. We thank  
790 Dr Yuan Yang for creating the NHE6-FLAG plasmid and the UTSW Whole Brain Microscopy  
791 Facility (WBMF) in the Department of Neurology and Neurotherapeutics for assistance with slide  
792 scanning. The WBMF is supported by the Texas Institute for Brain Injury and Repair (TIBIR).

793 John Shelton and the UT Southwestern's Histopathology Core provided help with paraffin  
794 sectioning as well as H&E and Thioflavin S staining. We thank Wolfgang Scholz for providing  
795 EMD87580.

796

## 797 **AUTHOR CONTRIBUTION**

798 Theresa Pohlkamp designed and performed research, analyzed data, and wrote the  
799 paper. Xunde Xian, designed and performed research, analyzed data, reviewed and edited the  
800 paper. Connie H Wong, designed and performed research, analyzed data, illustrated figures,  
801 reviewed and edited the paper. Murat S Durakoglugil, designed and performed research,  
802 analyzed data, reviewed and edited the paper. Takaomi Saido provided the humanized *App<sup>NL-F</sup>*  
803 mice. Jade Connor, performed research. Bret M Evers, performed research. Charles L White,  
804 analyzed data. Robert E Hammer, performed mouse manipulations to create the new *Slc9a6<sup>fl</sup>*  
805 mouse line. Joachim Herz, conceptualization, research design, resources, formal analysis,  
806 supervision, funding acquisition, validation, investigation, methodology, writing and editing the  
807 paper.

808

809 **FIGURE LEGENDS**

810 **Figure 1: ApoE4 Induces Endolysosomal Trafficking Delay.**

811 **(A)** pH regulation within the endolysosomal pathway. Upon receptor binding ApoE is  
812 endocytosed along with glutamate receptors (AMPA and NMDA receptors). Cargo that has  
813 entered the early endosome (EE) can undergo recycling through a fast direct route without  
814 further acidification (fast recycling) or through slower sorting pathways that require further  
815 acidification (Casey et al., 2010; Naslavsky and Caplan, 2018). While lipid components are  
816 targeted to the lysosome, the majority of receptors, as well as ApoE, remain in endosomal  
817 compartments at the cellular periphery where they rapidly move back to the surface (Heeren et  
818 al., 1999). The increasingly acidic luminal pH is illustrated as a color gradient and depicted on  
819 the left. **(B)** In the presence of ApoE4 early endosomal trafficking and fast recycling are delayed.  
820 At the pH of the EE, ApoE4 is near its isoelectric point where solubility is reduced (Wintersteiner  
821 and Abramson, 1933), impairing receptor dissociation and resulting in delayed endosomal  
822 maturation with a concomitant entrapment of co-endocytosed glutamate receptors. Endosomal  
823 pH is regulated by the vesicular ATPase and the counterregulatory action of the proton leakage  
824 channel NHE6. NHE6 is an antiporter that exchanges a Na<sup>+</sup> or K<sup>+</sup> ion for each proton. As the  
825 pH decreases, ligands dissociate from their receptors allowing the EE to mature. If dissociation  
826 is delayed, as in case of ApoE4, endosomal trafficking is arrested, leading to progressive  
827 acidification as Na<sup>+</sup>, K<sup>+</sup> and Cl<sup>-</sup> ions continue to enter the endosome to maintain charge  
828 neutrality while also drawing in water molecules due to osmotic pressure. We thus propose a  
829 model in which delayed ApoE4-receptor dissociation prevents early endosomal maturation and  
830 causes osmotic swelling while the pH continues to decrease until dissociation occurs. **(C)**  
831 Accelerated endosomal acidification by inhibition of the proton leak channel NHE6 resolves  
832 ApoE4 accumulation, promotes rapid receptor dissociation and promotes the vesicle entry into  
833 the lysosomal delivery or recycling pathways.

834

835 **Figure 2: Generation of *Slc9a6*<sup>fl</sup> and *Slc9a6*<sup>-/-</sup> Mice.**

836 **(A)** Gene targeting strategy. LoxP sites were introduced to flank the first exon (E1) of  
837 *Slc9a6* (located on the X-Chromosome) by gene targeting in embryonic stem cells. The  
838 targeting construct contained a long arm of homology (LA, grey) upstream of the first loxP site

839 and the first exon. A loxP/FRT-flanked neomycin resistance cassette was cloned downstream of  
840 the first exon, followed by a short arm of homology (SA, grey). The targeted locus is shown  
841 below. Targeted stem cells were used to generate chimeric *Slc9a6<sup>fl</sup>* mice. Germline NHE6  
842 knockout mice (NHE6<sup>-/-</sup> (female), NHE6<sup>y/-</sup> (male); rec indicates recombined allele) were  
843 generated by breeding the *Slc9a6<sup>fl</sup>* line with Meox-Cre mice. **(B)** Genotyping of wildtype (wt, +),  
844 floxed (fl), and recombined (rec, -) NHE6 alleles. The PCR amplified regions are indicated in  
845 panel A. The wildtype and floxed allele PCR products differ by 50 bp (270 for floxed, 220 for  
846 wildtype). **(C)** Western blot showing brain lysates (left) of different NHE6 genotypes after Meox-  
847 Cre induced germline recombination. **(D)** Mouse embryonic fibroblasts from *Slc9a6<sup>-</sup>* and control  
848 littermate were infected with Vamp3-pHluorin2 and excited at 408 and 488 nm with emission  
849 measured at 510 nm. **(E)** Vesicular pH measured using a standard curve was significantly  
850 decreased in *Slc9a6<sup>-</sup>* fibroblasts. Data is expressed as mean  $\pm$  SEM. Statistical analysis was  
851 performed using Student *t*-test. (\*\**p*<0.01) **(F)** The percent of vesicles with pH >6.4 is  
852 significantly decreased in *Slc9a6<sup>-</sup>* fibroblasts. **(G)** CAG-Cre<sup>ERT2</sup> activity after tamoxifen  
853 application in a reporter mouse line expressing tdTomato. Cre<sup>ERT2</sup> recombination activity without  
854 (left panel) or with (middle panel) tamoxifen application in the CAG-Cre<sup>ERT2</sup>-line bred with  
855 Rosa26<sup>floxStop-tdTomato</sup> line. After tamoxifen induction CreERT2 activity led to a robust tdTomato  
856 signal in the hippocampus (middle panel). Pyramidal neurons in the CA1 pyramidal cell layer  
857 (PCL) (middle panel) are shown magnified in the right panel.

858

859 **Figure 3: Long-Term NHE6-Deficiency Induced After Purkinje Cell Maturation**  
860 **Causes Purkinje Cell-loss.**

861 **(A)** Experimental timeline for B, mice were injected with tamoxifen at 2 months; after one month  
862 the brains were analyzed for NHE6 expression (Tam = tamoxifen, Exp. = experiment, mo. =  
863 months). **(B)** Western blot showing the efficiency of tamoxifen-induced NHE6 knockout in  
864 different brain regions (CA1, CA3, dentate gyrus, cortex, and cerebellum). The knockout  
865 efficiency differed between brain regions, it was 80 $\pm$ 2% in CA1, 82 $\pm$ 5.7% in the CA3, 67 $\pm$ 6.8%  
866 in the dentate gyrus, 65 $\pm$ 11.2% in the cortex, and 74 $\pm$ 4.7% in the cerebellum. A total of 3 brains  
867 in each group were examined. **(C-F)** NHE6 deficiency leads to cerebellar Purkinje cell loss in  
868 germline (*Slc9a6<sup>-</sup>*, C) and conditional (*Slc9a6<sup>fl</sup>;CAG-Cre<sup>ERT2</sup>*, D-F) knockout mice. *Slc9a6<sup>+</sup>*  
869 includes both female wildtypes (*Slc9a6<sup>+/+</sup>*) and male wildtypes (*Slc9a6<sup>y/+</sup>*) mice. *Slc9a6<sup>-</sup>* includes

870 both female knockouts (*Slc9a6*<sup>-/-</sup>) and male knockouts (*Slc9a6*<sup>y/-</sup>) mice. In addition, *Slc9a6*<sup>fl</sup> mice  
871 includes both female *Slc9a6*<sup>fl/fl</sup> and male *Slc9a6*<sup>y/fl</sup>. The timeline shows that *Slc9a6*<sup>fl</sup>;CAG-  
872 *Cre*<sup>ERT2</sup> and control mice were tamoxifen-injected at two months and analyzed one year after  
873 (D). Calbindin was fluorescently labeled to highlight Purkinje cells in the cerebellum. Massive  
874 loss of Purkinje cells was found in *Slc9a6*<sup>-</sup> (C, lower panel), compared to wildtype *Slc9a6*<sup>+</sup>  
875 control (C, upper panel). Long-term loss of NHE6, induced after Purkinje cell maturation at two  
876 months of age, also led to massive Purkinje cells-loss when mice were examined one year after  
877 NHE6-ablation (E, lower panel). **(F)** Quantification of Purkinje cell-loss in the cerebellum of  
878 *Slc9a6*<sup>fl</sup>;CAG-*Cre*<sup>ERT2</sup> mice. Values are expressed as mean ± SEM from 4 independent  
879 experiments. Statistical analysis was performed using Student *t*-test. \**p*<0.05.

880

881 **Figure 4: NHE6 Deficiency Alleviates ApoE4-Impaired Surface Trafficking Deficits**  
882 **of Apoer2 and Glutamate Receptors.**

883 **(A)** Timeline for the receptor surface expression assay applied for the experiments shown  
884 in B-F. Primary neurons were treated with naturally secreted ApoE3 or ApoE4 and/or Reelin  
885 before they underwent surface biotinylation. **(B-F)** Wildtype and *Slc9a6*<sup>-</sup> primary neurons were  
886 prepared from littermates and used in the receptor surface expression assay described in A. .  
887 *Slc9a6*<sup>+</sup> includes both female wildtypes (*Slc9a6*<sup>+/+</sup>) and male wildtypes (*Slc9a6*<sup>y/+</sup>) mice. *Slc9a6*<sup>-</sup>  
888 includes both female knockouts (*Slc9a6*<sup>-/-</sup>) and male knockouts (*Slc9a6*<sup>y/-</sup>) mice. **(B)** NHE6-  
889 deficiency was confirmed via Western blot, β-actin was used as loading control. **(C-F)** ApoE-  
890 conditioned media treatment reduces the surface expression of Apoer2 and glutamate receptors  
891 in presence of Reelin in primary neurons. Receptor surface levels show a stronger reduction  
892 with ApoE4 than ApoE3. NHE6 depletion counteracts the ApoE4-induced reduction of receptor  
893 surface expression. Cell surface biotinylation assay was performed for Apoer2 (C), GluN2B (D),  
894 GluA1 (E) and GluA2/3 (F). Total levels were analyzed by immunoblotting of whole cell lysates  
895 against the same antibodies. β-actin was used as loading control. Quantitative analysis of  
896 immunoblot signals is shown in the lower panels (C-F). All data are expressed as mean ± SEM  
897 from 3 independent experiments. \**p* < 0.05, \*\**p* < 0.01, \*\*\**p* < 0.005. Statistical analysis was  
898 performed using one-way ANOVA and Dunnett's post hoc test **(C-F)**.

899

900 **Figure 5: Effect of Conditional NHE6 Knockout on Reelin-potentiated Synaptic**  
901 **Plasticity.**

902 **(A-H)** Conditional knockout of NHE6 restores Reelin-enhanced long-term potentiation  
903 (LTP) in *Apoe*<sup>APOE4</sup> mice. Reelin facilitated induction of LTP in *Apoe*<sup>APOE3</sup> **(A, E)**, but not  
904 *Apoe*<sup>APOE4</sup> **(C, G)** control (*Slc9a6*<sup>fl</sup>) mice. *Slc9a6*-deficiency in *Apoe*<sup>APOE3</sup> mice caused a  
905 reduction in Reelin enhanced LTP, such that it is not significantly different from the control LTP  
906 **(B, F)**. Importantly, in *Apoe*<sup>APOE4</sup>;*Slc9a6*<sup>fl</sup>;*CAG-Cre*<sup>ERT2</sup> mice Reelin was able to enhance theta-  
907 burst induced potentiation **(D, H)**. Hippocampal slices were prepared from 3 months old double  
908 mutant mice with either human *Apoe*<sup>APOE3</sup> or *Apoe*<sup>APOE4</sup> crossed with *Slc9a6* conditional  
909 knockout mice (*Slc9a6*<sup>fl</sup>;*CAG-Cre*<sup>ERT2</sup>, tamoxifen-injections at 6-8 weeks). Extracellular field  
910 recordings were performed in slices treated with or without Reelin. Theta burst stimulation (TBS)  
911 was performed after 20 minutes of stable baseline. Representative traces are shown in each  
912 panel, before TBS induction (black) and 40 min after TBS (grey). **(E-H)** Quantitative analysis of  
913 normalized fEPSP slopes at time intervals as indicated. **(I, J)** Input output curves of *Apoe*<sup>APOE3</sup>  
914 **(I)** and *Apoe*<sup>APOE4</sup>**(J)** mice with or without *Slc9a6*<sup>fl</sup>;*CAG-Cre*<sup>ERT2</sup>. *Slc9a6*<sup>fl</sup> mice includes both  
915 female *Slc9a6*<sup>fl/fl</sup> and male *Slc9a6*<sup>y/fl</sup> mice. *Apoe* mice are homozygous for APOE3 or APOE4. All  
916 data are expressed as mean ± SEM. N-numbers for each genotype group and treatment are  
917 indicated in panels A-D. \*p < 0.05. Statistical analysis was performed using Student *t*-test.

918

919 **Figure 6: NHE Inhibition or NHE6 Knockdown Does Not Alter BACE1 Activity in**  
920 **Primary Neurons.**

921 **(A,B)** Pan-NHE inhibition by EMD87580 or lentiviral knockdown of *Slc9a6* (NHE6) did not  
922 alter BACE1 activity in primary neurons of *AppSwe* mice (Tg2576). **(A)** DIV10 primary neurons  
923 were treated with  $\gamma$ -secretase inhibitor L-685458, EMD87580, and/or ApoE4 (as indicated) and  
924 harvested for immunoblotting against A $\beta$ -containing C-terminal fragment of APP ( $\beta$ CTF).  $\beta$ -actin  
925 was blotted as loading control. Bar graph shows the statistics of n = 3 experiments. **(B)** Primary  
926 neurons of *AppSwe* mice were infected with lentivirus for shRNA expression directed against  
927 *Slc9a6*(NHE6) (sh*Slc9a6*) or a scramble control sequence (-) at DIV7. At DIV13 neurons were  
928 treated with L-685458 overnight and harvested for immunoblotting against NHE6 and  $\beta$ CTF on  
929 DIV14. RAP was blotted as loading control. Bar graph shows the statistics of n = 6 experiments.

930 All data are expressed as mean  $\pm$  SEM. Statistical analysis was performed using Student *t*-test.  
931 n.s. = not significant.

932

933 **Figure 7: NHE6-Deficiency Decreases Plaque Formation in Both *App*<sup>NL-F</sup> and *App*<sup>NL-F</sup>;  
934 *F*; *ApoE*<sup>APOE4</sup> Mice.**

935 **(A,B)** NHE6-deficient *App*<sup>NL-F</sup> and control *App*<sup>NL-F</sup> mice were analyzed for plaque  
936 deposition at an age of 12 months. Thioflavin S staining was performed to visualize plaques.  
937 Plaques were found more frequently in the control *App*<sup>NL-F</sup> mice (left panel in **A**), magnifications  
938 of the boxed areas are shown in the two middle panels. The plaque load between *Slc9a6*<sup>-</sup> mice  
939 and control littermates (all *App*<sup>NL-F</sup>) was compared and analyzed. **(B)** In the *Slc9a6*<sup>-</sup> littermates  
940 the plaque number was reduced, when compared to controls. **(C-D)** *Slc9a6*<sup>fl</sup>;CAG-  
941 *Cre*<sup>ERT2</sup>; *App*<sup>NL-F</sup>; *ApoE*<sup>APOE4</sup> and *Slc9a6*<sup>fl</sup>; *App*<sup>NL-F</sup>; *ApoE*<sup>APOE4</sup> mice were analyzed for plaque  
942 deposition. NHE6 was ablated at two months and brains were analyzed at 13.5-16 months.  
943 4G8-immunolabeling against A $\beta$  was performed to visualize plaques. In *App*<sup>NL-F</sup>; *ApoE*<sup>APOE4</sup> mice  
944 conditional *Slc9a6* knockout caused a reduction in plaque load compared to the *Slc9a6*<sup>fl</sup> control  
945 littermates **(C)**. Magnifications of the boxed areas in C are shown in the middle. **(D)** Plaque load  
946 was analyzed and compared between *Slc9a6*<sup>fl</sup>;CAG-*Cre*<sup>ERT2</sup> mice and floxed control littermates.  
947 **I** Hematoxylin and eosin staining (H&E) was performed to investigate for gross anatomic  
948 abnormalities in the *Slc9a6*<sup>fl</sup>;CAG-*Cre*<sup>ERT2</sup>; *App*<sup>NL-F</sup>; *ApoE*<sup>APOE4</sup> and *Slc9a6*<sup>fl</sup>; *App*<sup>NL-F</sup>; *ApoE*<sup>APOE4</sup>  
949 mice. **(F-I)** Brain area **(F)**, cortical thickness **(G)**, hippocampal (HC) area **(H)**, and CA1 thickness  
950 **(I)** were analyzed. Student *t*-test did not reveal a significant difference. Plaques were  
951 differentiated by size or staining density as described in detail in the supplements **(Figure 7 –**  
952 **Figure Supplement 2)**. Labeled plaques were analyzed by a blinded observer. All data are  
953 expressed as mean  $\pm$  SEM. **(B)** *Slc9a6*<sup>-</sup> n=5, control n=8, **(C)** *Slc9a6*<sup>fl</sup> n=8, *Slc9a6*<sup>fl</sup>;CAG-*Cre*<sup>ERT2</sup>  
954 n=8), in **(F-I)** derived from n=5 (*Slc9a6*<sup>fl</sup>) and n=6 (*Slc9a6*<sup>fl</sup>;CAG-*Cre*<sup>ERT2</sup>) animals. \*p < 0.05.  
955 \*\*p<0.01, \*\*\*p<0.005. *Slc9a6*<sup>+</sup> represents both female wildtypes (*Slc9a6*<sup>+/+</sup>) and male wildtypes  
956 (*Slc9a6*<sup>y/+</sup>). *Slc9a6*<sup>-</sup> represents both female knockouts (*Slc9a6*<sup>-/-</sup>) and male knockouts (*Slc9a6*<sup>y/-</sup>).  
957 In addition, *Slc9a6*<sup>fl</sup> mice includes both female *Slc9a6*<sup>fl/fl</sup> and male *Slc9a6*<sup>y/fl</sup> mice. *ApoE* mice are  
958 homozygous for APOE4 (*ApoE*<sup>APOE4</sup>). *App*<sup>NL-F</sup> mice are homozygous for human NL-F knockin  
959 mutation (*App*<sup>NL-F/NL-F</sup>). Statistical analysis was performed using two-way ANOVA with Sidak's  
960 post-hoc test **(B and D)** and Student *t*-test **(F-I)**.

961  
962 **Figure 7 – Figure Supplement 1: Gross Anatomical Brain Structure in *Slc9a6* Mice.**

963 (A) Hematoxylin and eosin staining (H&E) was performed to investigate for gross  
964 anatomic abnormalities in the *Slc9a6*<sup>-</sup>;*App*<sup>NL-F</sup> and *App*<sup>NL-F</sup> mice. Structures representing  
965 plaques were found in the *App*<sup>NL-F</sup> control groups (magnified example is shown in the middle  
966 panel). (B-E) Brain area (B), cortical thickness (C), hippocampal (HC) area (D), and CA1  
967 thickness (E) were analyzed. All data are expressed as mean ± SEM. Student *t*-test did not  
968 reveal significant differences, n=3 (control) and n=4 (*Slc9a6*<sup>-</sup>). *Slc9a6*<sup>+</sup> represents both female  
969 wildtypes (*Slc9a6*<sup>+/+</sup>) and male wildtypes (*Slc9a6*<sup>+/+</sup>). *Slc9a6*<sup>-</sup> represents both female knockouts  
970 (*Slc9a6*<sup>-/-</sup>) and male knockouts (*Slc9a6*<sup>Y/-</sup>). *App*<sup>NL-F</sup> mice are homozygous for human NL-F  
971 knockin mutation (*App*<sup>NL-F/NL-F</sup>).

972  
973 **Figure 7 – Figure Supplement 2: Example of Thioflavin S Stained Plaques for**  
974 **Quantification.**

975 Different types of Thioflavin S stained plaques and 4G8-immunoreactive accumulations in  
976 *App*<sup>NL-F</sup> brains are shown. Different sizes of plaques were grouped together for quantification  
977 Thioflavin S labeled plaques (Figure 7 and Figure 7 – Figure Supplement 3). Plaques bigger  
978 in diameter than 20µm with a dense core were defined as big. Medium sized plaques had a  
979 diameter between 10-20µm with a dense core. Small plaques were smaller than 10µm and often  
980 represented individual cells. 4G8-labeled plaques were differentiated by diffuse or dense  
981 appearance as depicted in the examples.

982  
983 **Figure 7 – Figure Supplement 3: NHE6-Deficiency Decreases Plaque Formation in**  
984 **Both *App*<sup>NL-F</sup> and *App*<sup>NL-F</sup>;*ApoE*<sup>APOE4</sup> Mice.**

985 (A-B) NHE6-deficient *App*<sup>NL-F</sup> and control *App*<sup>NL-F</sup> mice were analyzed for plaque  
986 deposition at an age of 12 months. 4G8-immunolabeling against Aβ (A) visualized more plaques  
987 in the control *App*<sup>NL-F</sup> mice. The plaque load between *Slc9a6*<sup>-</sup> mice and control littermates (all  
988 *App*<sup>NL-F</sup>) was compared and analyzed (B). In the *Slc9a6*<sup>-</sup> littermates the plaque number was  
989 reduced, when compared to controls. (C-E) Soluble (TBS) and insoluble (GuHCl and 70% FA)  
990 Aβ fractions of cortical lysates were analyzed by commercial ELISA. 1.5-year-old *Slc9a6*<sup>-</sup> mice

991 showed less insoluble A $\beta$  than their control littermates (all *App*<sup>NL-F</sup>). **(F-G)** *Slc9a6*<sup>fl</sup>;CAG-  
992 *Cre*<sup>ERT2</sup>; *App*<sup>NL-F</sup>; *ApoE*<sup>APOE4</sup> and *Slc9a6*<sup>fl</sup>; *App*<sup>NL-F</sup>; *ApoE*<sup>APOE4</sup> mice were analyzed for plaque  
993 deposition. NHE6 was ablated at two months and brains were analyzed at 13.5-16 months.  
994 Thioflavin S staining was performed to visualize plaques. With *App*<sup>NL-F</sup>; *ApoE*<sup>APOE4</sup> background  
995 the *Slc9a6*<sup>fl</sup>;CAG-*Cre*<sup>ERT2</sup> mice had a reduced plaque load compared to the *Slc9a6*<sup>fl</sup> control mice  
996 (left panel in **F**). Magnifications of the boxed areas in left panel are shown in the middle. **(G)**  
997 Plaque load was analyzed and compared between *Slc9a6*<sup>fl</sup>;CAG-*Cre*<sup>ERT2</sup> mice and floxed control  
998 littermates. Plaques were differentiated by size or staining density as described in detail in the  
999 supplements (**Figure 7 – Figure Supplement 2**). Labeled plaques were analyzed by a blinded  
1000 observer (**B, G**). All data (immunohistochemistry: *Slc9a6*<sup>-</sup> n=5, control n=4, *Slc9a6*<sup>fl</sup> n=10,  
1001 *Slc9a6*<sup>fl</sup>;CAG-*Cre*<sup>ERT2</sup> n=12; biochemistry: *Slc9a6*<sup>-</sup> n=11, control n=7) are expressed as mean  $\pm$   
1002 SEM. \*p < 0.05. \*\*p<0.01, \*\*\*p<0.005. *Slc9a6*<sup>+</sup> represents both female wildtypes (*Slc9a6*<sup>+/+</sup>) and  
1003 male wildtypes (*Slc9a6*<sup>+/+</sup>). *Slc9a6*<sup>-</sup> represents both female knockouts (*Slc9a6*<sup>-/-</sup>) and male  
1004 knockouts (*Slc9a6*<sup>y/-</sup>). In addition, *Slc9a6*<sup>fl</sup> mice includes both female *Slc9a6*<sup>fl/fl</sup> and male  
1005 *Slc9a6*<sup>y/fl</sup> mice. *ApoE* mice are homozygous for APOE4. *App*<sup>NL-F</sup> mice are homozygous for  
1006 human NL-F knockin mutation (*App*<sup>NL-F/NL-F</sup>). Statistical analysis was performed using two-way  
1007 ANOVA with Sidak's post-hoc test.

1008

1009 **Figure 8. Age Dependent Increase in Plaque Load is abolished in *Slc9a6*<sup>fl</sup>;CAG-**  
1010 ***Cre*<sup>ERT2</sup>; *App*<sup>NL-F</sup>; *ApoE*<sup>APOE4</sup> Mice.**

1011 **(A-E)** *Slc9a6*<sup>fl</sup>;CAG-*Cre*<sup>ERT2</sup>; *App*<sup>NL-F</sup>; *ApoE*<sup>APOE4</sup> and *Slc9a6*<sup>fl</sup>; *App*<sup>NL-F</sup>; *ApoE*<sup>APOE4</sup> mice were  
1012 analyzed for plaque deposition. NHE6 was ablated at two months and brains were analyzed at  
1013 13.5-16 months. 4G8-immunolabeling against A $\beta$  (**A,B**) and Thioflavin S staining (**C-E**) were  
1014 performed to visualize plaques (**Figure 7C and Figure 7 – Figure Supplement 3F**). Plaque  
1015 load was analyzed and compared between *Slc9a6*<sup>fl</sup>;CAG-*Cre*<sup>ERT2</sup> mice and floxed control  
1016 littermates. Plaques were differentiated by staining intensity (**A, B**) or size (**C-E**) as described in  
1017 the supplements (**Figure 7 – Figure Supplement 2**). In the time range analyzed, plaque load  
1018 increased by age in control, but not in *Slc9a6*<sup>fl</sup>;CAG-*Cre*<sup>ERT2</sup> mice. Plaques were analyzed by a  
1019 blinded observer. Plaque count (*Slc9a6*<sup>fl</sup>;CAG-*Cre*<sup>ERT2</sup> n=8, *Slc9a6*<sup>fl</sup> n=8 for **A** and **B**;  
1020 *Slc9a6*<sup>fl</sup>;CAG-*Cre*<sup>ERT2</sup> n=12; *Slc9a6*<sup>fl</sup> n=10 in **C-E**) is plotted against age of mice. *Slc9a6*<sup>fl</sup> mice

1021 includes both female *Slc9a6<sup>fl/fl</sup>* and male *Slc9a6<sup>y/fl</sup>* mice. *ApoE* mice are homozygous for APOE4.  
1022 *App<sup>NL-F</sup>* mice are homozygous for human NL-F knockin mutation (*App<sup>NL-F/NL-F</sup>*).

1023  
1024 **Figure 9. Microglia and Astrocytes Surround Plaques in Both *App<sup>NL-F</sup>* Control and**  
1025 ***App<sup>NL-F</sup>;Slc9a6<sup>-</sup>* Brains**

1026 **(A-B)** Co-labeling of microglia (Iba1, green, **A**) or astrocytes (GFAP, green, **B**) with A $\beta$   
1027 (6E10, red) in brain slices of *App<sup>NL-F</sup>* and *App<sup>NL-F</sup>;Slc9a6<sup>-</sup>* mice. **(C)** Quantification of plaques in  
1028 control and *Slc9a6<sup>-</sup>* brain slices. **(D)** Bar graph showing the intensity density of Iba1/6E10 as  
1029 quantitative measure of microglia surrounding plaques. **(E)** Statistical analysis of 6E10 positive  
1030 microglia and **(F)** the intensity of 6E10 signal within microglia. **(G)** Bar graph showing the  
1031 intensity density of GFAP/A $\beta$  as quantitative measure of astrocytes surrounding plaques. Data  
1032 were analyzed by a blinded observer. All data are expressed as mean  $\pm$  SEM. Data were  
1033 obtained from n=4 (control) and n=5 (*Slc9a6<sup>-</sup>*) mice **(A-G)**. **(D)** n=33 (control) and n=23 (*Slc9a6<sup>-</sup>*)  
1034 plaques were analyzed, in **(E)** n=22 (control) and n=24 (*Slc9a6<sup>-</sup>*) microscopical pictures were  
1035 analyzed, in **(F)** n=31 (control) and n=38 (*Slc9a6<sup>-</sup>*) 6E10 positive (defined as signal intensity  
1036 above 500) microglia were analyzed, in **(G)** n=33 (control) and n=18 (*Slc9a6<sup>-</sup>*) plaques were  
1037 analyzed. Student *t*-test revealed a difference in **C** (\*\*p<0.01) and did not reveal significant  
1038 differences in **D-G**. *Slc9a6<sup>+</sup>* represents both female wildtypes (*Slc9a6<sup>+/+</sup>*) and male wildtypes  
1039 (*Slc9a6<sup>y/+</sup>*). *Slc9a6<sup>-</sup>* represents both female knockouts (*Slc9a6<sup>-/-</sup>*) and male knockouts (*Slc9a6<sup>y/-</sup>*).  
1040 *App<sup>NL-F</sup>* mice are homozygous for human NL-F knockin mutation (*App<sup>NL-F/NL-F</sup>*).

1041  
1042  
1043 **Figure 9 – Figure Supplement 1: NHE6-Deficiency Causes an Increase in Iba1 and**  
1044 **GFAP Immunoreactivity in Both *App<sup>NL-F</sup>* and *App<sup>NL-F</sup>;ApoE<sup>APOE4</sup>* mice.**

1045 **(A)** Immunohistochemistry against glial fibrillary acidic protein (GFAP) and ionized calcium-  
1046 binding adapter molecule (Iba1) was performed on brain slices obtained from one-year-old  
1047 *App<sup>NL-F</sup>* mice deficient for NHE6 (*App<sup>NL-F</sup>;Slc9a6<sup>-</sup>*) and control littermates (*App<sup>NL-F</sup>*). GFAP (upper  
1048 panels) and Iba1 (lower panels) immunoreactivity was increased in NHE6-deficient *App<sup>NL-F</sup>* mice  
1049 when compared to NHE6 expressing controls. **(B)** *Slc9a6<sup>fl</sup>;CAG-Cre<sup>ERT2</sup>;App<sup>NL-F</sup>;ApoE<sup>APOE4</sup>* and  
1050 *Slc9a6<sup>fl</sup>;App<sup>NL-F</sup>;ApoE<sup>APOE4</sup>* mice were analyzed for immunoreactivity GFAP and Iba1. Mice were

1051 injected with tamoxifen at two months and brain slices obtained from 13.5-16 months old mice.  
1052 GFAP (upper panels) and Iba1 (lower panels) immunoreactivity was increased in NHE6-  
1053 deficient  $App^{NL-F}; ApoE^{APOE4}$  mice when compared to NHE6 expressing controls. **(C-F)** Intensity  
1054 of the staining in various areas was compared for GFAP **(C)** and Iba1 **(D)** in  $App^{NL-F}; Slc9a6^{-}$  and  
1055  $App^{NL-F}$  mice. Intensity of the staining for GFAP **(E)** and Iba1 **(F)** in  $Slc9a6^{fl}; CAG-Cre^{ERT2}; App^{NL-F}; ApoE^{APOE4}$   
1056 and  $Slc9a6^{fl}; App^{NL-F}; ApoE^{APOE4}$  mice. Analysis was performed by a blinded  
1057 observer. 'White matter' comprises corpus callosum, cingulum and external capsule. All data  
1058 ( $Slc9a6^{-}$  n=5; control n=4;  $Slc9a6^{fl}; CAG-Cre^{ERT2}$  n=6;  $Slc9a6^{fl}$  n=8) are expressed as mean  $\pm$   
1059 SEM. \*p < 0.05. \*\*p<0.01, \*\*\*p<0.005.  $Slc9a6^{+}$  represents both female wildtypes ( $Slc9a6^{+/+}$ ) and  
1060 male wildtypes ( $Slc9a6^{y/+}$ ).  $Slc9a6^{-}$  represents both female knockouts ( $Slc9a6^{-/-}$ ) and male  
1061 knockouts ( $Slc9a6^{y/-}$ ). In addition,  $Slc9a6^{fl}$  mice includes both female  $Slc9a6^{fl/fl}$  and male  
1062  $Slc9a6^{y/fl}$  mice. For the  $Cag-Cre^{ERT2}$ ,  $Cre^{+}$  indicates the absence of Cre ( $Slc9a6^{fl}$  alone) and  
1063  $Cag-Cre^{ERT2}$  indicates the presence of Cre ( $Slc9a6^{fl}; CAG-Cre^{ERT2}$ ), which are both injected with  
1064 Tamoxifen at 2 months of age.  $ApoE$  mice are homozygous for APOE4.  $App^{NL-F}$  mice are  
1065 homozygous for human NL-F knockin mutation ( $App^{NL-F/NL-F}$ ). Statistical analysis was performed  
1066 using Student *t*-test.

1067

1068 **Figure 9 – Figure Supplement 2: Examples of Plaques Surrounded by Microglia**  
1069 **and Astrocytes.**

1070 **(A)** Co-labeling of microglia (Iba1, green) and A $\beta$  (6E10, red) in brain slices of  $App^{NL-F}$   
1071 and  $App^{NL-F}; Slc9a6^{-}$  mice. **(B)** Co-labeling of astrocytes (GFAP, green) and A $\beta$  (6E10, red) in  
1072 brain slices of  $App^{NL-F}$  and  $App^{NL-F}; Slc9a6^{-}$  mice.  $Slc9a6^{+}$  represents both female wildtypes  
1073 ( $Slc9a6^{+/+}$ ) and male wildtypes ( $Slc9a6^{y/+}$ ).  $Slc9a6^{-}$  represents both female knockouts ( $Slc9a6^{-/-}$ )  
1074 and male knockouts ( $Slc9a6^{y/-}$ ).  $App^{NL-F}$  mice are homozygous for human NL-F knockin mutation  
1075 ( $App^{NL-F/NL-F}$ ).

1076

1077

1078

## References

- 1079  
1080
- 1081 Arboleda-Velasquez, J.F., Lopera, F., O'Hare, M., Delgado-Tirado, S., Marino, C., Chmielewska,  
1082 N., Saez-Torres, K.L., Amarnani, D., Schultz, A.P., Sperling, R.A., *et al.* (2019). Resistance to  
1083 autosomal dominant Alzheimer's disease in an APOE3 Christchurch homozygote: a case report.  
1084 *Nature medicine* 25, 1680-1683.
- 1085 Basu, S.K., Goldstein, J.L., Anderson, G.W., and Brown, M.S. (1976). Degradation of cationized  
1086 low density lipoprotein and regulation of cholesterol metabolism in homozygous familial  
1087 hypercholesterolemia fibroblasts. *Proceedings of the National Academy of Sciences of the*  
1088 *United States of America* 73, 3178-3182.
- 1089 Beffert, U., Weeber, E.J., Durudas, A., Qiu, S., Masiulis, I., Sweatt, J.D., Li, W.P., Adelmann, G.,  
1090 Frotscher, M., Hammer, R.E., *et al.* (2005). Modulation of synaptic plasticity and memory by  
1091 Reelin involves differential splicing of the lipoprotein receptor Apoer2. *Neuron* 47, 567-579.
- 1092 Benilova, I., Karran, E., and De Strooper, B. (2012). The toxic Abeta oligomer and Alzheimer's  
1093 disease: an emperor in need of clothes. *Nature neuroscience* 15, 349-357.
- 1094 Braybrooke, J.P., Spink, K.G., Thacker, J., and Hickson, I.D. (2000). The RAD51 family  
1095 member, RAD51L3, is a DNA-stimulated ATPase that forms a complex with XRCC2. *The*  
1096 *Journal of biological chemistry* 275, 29100-29106.
- 1097 Brich, J., Shie, F.S., Howell, B.W., Li, R., Tus, K., Wakeland, E.K., Jin, L.W., Mumby, M.,  
1098 Churchill, G., Herz, J., *et al.* (2003). Genetic modulation of tau phosphorylation in the mouse.  
1099 *The Journal of neuroscience : the official journal of the Society for Neuroscience* 23, 187-192.
- 1100 Caporaso, G.L., Takei, K., Gandy, S.E., Matteoli, M., Mundigl, O., Greengard, P., and De  
1101 Camilli, P. (1994). Morphologic and biochemical analysis of the intracellular trafficking of the  
1102 Alzheimer beta/A4 amyloid precursor protein. *The Journal of neuroscience : the official journal*  
1103 *of the Society for Neuroscience* 14, 3122-3138.
- 1104 Casey, J.R., Grinstein, S., and Orlowski, J. (2010). Sensors and regulators of intracellular pH.  
1105 *Nature reviews Molecular cell biology* 11, 50-61.
- 1106 Cataldo, A.M., Peterhoff, C.M., Troncoso, J.C., Gomez-Isla, T., Hyman, B.T., and Nixon, R.A.  
1107 (2000). Endocytic pathway abnormalities precede amyloid beta deposition in sporadic  
1108 Alzheimer's disease and Down syndrome: differential effects of APOE genotype and presenilin  
1109 mutations. *The American journal of pathology* 157, 277-286.
- 1110 Chen, Y., Beffert, U., Ertunc, M., Tang, T.S., Kavalali, E.T., Bezprozvanny, I., and Herz, J.  
1111 (2005). Reelin modulates NMDA receptor activity in cortical neurons. *The Journal of*  
1112 *neuroscience : the official journal of the Society for Neuroscience* 25, 8209-8216.
- 1113 Chen, Y., Durakoglugil, M.S., Xian, X., and Herz, J. (2010). ApoE4 reduces glutamate receptor  
1114 function and synaptic plasticity by selectively impairing ApoE receptor recycling. *Proceedings of*  
1115 *the National Academy of Sciences of the United States of America* 107, 12011-12016.
- 1116 Corder, E.H., Saunders, A.M., Risch, N.J., Strittmatter, W.J., Schmechel, D.E., Gaskell, P.C.,  
1117 Jr., Rimmler, J.B., Locke, P.A., Conneally, P.M., Schmechel, K.E., *et al.* (1994). Protective effect  
1118 of apolipoprotein E type 2 allele for late onset Alzheimer disease. *Nature genetics* 7, 180-184.

1119 D'Arcangelo, G., Nakajima, K., Miyata, T., Ogawa, M., Mikoshiba, K., and Curran, T. (1997).  
1120 Reelin is a secreted glycoprotein recognized by the CR-50 monoclonal antibody. *The Journal of*  
1121 *neuroscience : the official journal of the Society for Neuroscience* 17, 23-31.

1122 Davis, C.G., Goldstein, J.L., Sudhof, T.C., Anderson, R.G., Russell, D.W., and Brown, M.S.  
1123 (1987). Acid-dependent ligand dissociation and recycling of LDL receptor mediated by growth  
1124 factor homology region. *Nature* 326, 760-765.

1125 de Bouteiller, O., Merck, E., Hasan, U.A., Hubac, S., Benguigui, B., Trinchieri, G., Bates, E.E.,  
1126 and Caux, C. (2005). Recognition of double-stranded RNA by human toll-like receptor 3 and  
1127 downstream receptor signaling requires multimerization and an acidic pH. *The Journal of*  
1128 *biological chemistry* 280, 38133-38145.

1129 Deane, E.C., Ilie, A.E., Sisdahkhani, S., Das Gupta, M., Orłowski, J., and McKinney, R.A.  
1130 (2013). Enhanced recruitment of endosomal Na<sup>+</sup>/H<sup>+</sup> exchanger NHE6 into Dendritic spines of  
1131 hippocampal pyramidal neurons during NMDA receptor-dependent long-term potentiation. *The*  
1132 *Journal of neuroscience : the official journal of the Society for Neuroscience* 33, 595-610.

1133 Durakoglugil, M.S., Chen, Y., White, C.L., Kavalali, E.T., and Herz, J. (2009). Reelin signaling  
1134 antagonizes beta-amyloid at the synapse. *Proceedings of the National Academy of Sciences of*  
1135 *the United States of America* 106, 15938-15943.

1136 Eto, M., Watanabe, K., and Ishii, K. (1985). A rapid flat gel isoelectric focusing method for the  
1137 determination of apolipoprotein E phenotypes and its application. *Clinica chimica acta;*  
1138 *international journal of clinical chemistry* 149, 21-28.

1139 Fagan, A.M., Watson, M., Parsadanian, M., Bales, K.R., Paul, S.M., and Holtzman, D.M. (2002).  
1140 Human and murine ApoE markedly alters A beta metabolism before and after plaque formation  
1141 in a mouse model of Alzheimer's disease. *Neurobiology of disease* 9, 305-318.

1142 Fernandez-Monreal, M., Sanchez-Castillo, C., and Esteban, J.A. (2016). APPL1 gates long-term  
1143 potentiation through its plekstrin homology domain. *Journal of cell science* 129, 2793-2803.

1144 Fischer, A.H., Jacobson, K.A., Rose, J., and Zeller, R. (2008). Hematoxylin and eosin staining of  
1145 tissue and cell sections. *CSH protocols* 2008, pdb prot4986.

1146 Fox, R. (1996). Anti-malarial drugs: possible mechanisms of action in autoimmune disease and  
1147 prospects for drug development. *Lupus* 5 Suppl 1, S4-10.

1148 Gao, A.Y.L., Ilie, A., Chang, P.K.Y., Orłowski, J., and McKinney, R.A. (2019). A Christianson  
1149 syndrome-linked deletion mutation (Delta287ES288) in SLC9A6 impairs hippocampal neuronal  
1150 plasticity. *Neurobiology of disease* 130, 104490.

1151 Gao, S., Casey, A.E., Sargeant, T.J., and Makinen, V.P. (2018). Genetic variation within  
1152 endolysosomal system is associated with late-onset Alzheimer's disease. *Brain : a journal of*  
1153 *neurology* 141, 2711-2720.

1154 Guntern, R., Bouras, C., Hof, P.R., and Vallet, P.G. (1992). An improved thioflavine S method  
1155 for staining neurofibrillary tangles and senile plaques in Alzheimer's disease. *Experientia* 48, 8-  
1156 10.

1157 Haass, C., Kaether, C., Thinakaran, G., and Sisodia, S. (2012). Trafficking and proteolytic  
1158 processing of APP. *Cold Spring Harb Perspect Med* 2, a006270.

1159 Hayashi, S., and McMahon, A.P. (2002). Efficient recombination in diverse tissues by a  
1160 tamoxifen-inducible form of Cre: a tool for temporally regulated gene activation/inactivation in  
1161 the mouse. *Dev Biol* 244, 305-318.

1162 Heeren, J., Weber, W., and Beisiegel, U. (1999). Intracellular processing of endocytosed  
1163 triglyceride-rich lipoproteins comprises both recycling and degradation. *Journal of cell science*  
1164 112 ( Pt 3), 349-359.

1165 Hiesberger, T., Trommsdorff, M., Howell, B.W., Goffinet, A., Mumby, M.C., Cooper, J.A., and  
1166 Herz, J. (1999). Direct binding of Reelin to VLDL receptor and ApoE receptor 2 induces tyrosine  
1167 phosphorylation of disabled-1 and modulates tau phosphorylation. *Neuron* 24, 481-489.

1168 Hook, V.Y., Toneff, T., Aaron, W., Yasothornsrikul, S., Bunday, R., and Reisine, T. (2002). Beta-  
1169 amyloid peptide in regulated secretory vesicles of chromaffin cells: evidence for multiple  
1170 cysteine proteolytic activities in distinct pathways for beta-secretase activity in chromaffin  
1171 vesicles. *Journal of neurochemistry* 81, 237-256.

1172 Hsiao, K., Chapman, P., Nilsen, S., Eckman, C., Harigaya, Y., Younkin, S., Yang, F., and Cole,  
1173 G. (1996). Correlative memory deficits, Abeta elevation, and amyloid plaques in transgenic  
1174 mice. *Science* 274, 99-102.

1175 Huynh, T.V., Davis, A.A., Ulrich, J.D., and Holtzman, D.M. (2017). Apolipoprotein E and  
1176 Alzheimer's disease: the influence of apolipoprotein E on amyloid-beta and other amyloidogenic  
1177 proteins. *Journal of lipid research* 58, 824-836.

1178 Ilie, A., Boucher, A., Park, J., Berghuis, A.M., McKinney, R.A., and Orłowski, J. (2020). Assorted  
1179 dysfunctions of endosomal alkali cation/proton exchanger SLC9A6 variants linked to  
1180 Christianson syndrome. *The Journal of biological chemistry* 295, 7075-7095.

1181 Ilie, A., Gao, A.Y.L., Boucher, A., Park, J., Berghuis, A.M., Hoffer, M.J.V., Hilhorst-Hofstee, Y.,  
1182 McKinney, R.A., and Orłowski, J. (2019). A potential gain-of-function variant of SLC9A6 leads to  
1183 endosomal alkalization and neuronal atrophy associated with Christianson Syndrome.  
1184 *Neurobiology of disease* 121, 187-204.

1185 Jovic, M., Sharma, M., Rahajeng, J., and Caplan, S. (2010). The early endosome: a busy  
1186 sorting station for proteins at the crossroads. *Histology and histopathology* 25, 99-112.

1187 Knopman, D.S., Amieva, H., Petersen, R.C., Chetelat, G., Holtzman, D.M., Hyman, B.T., Nixon,  
1188 R.A., and Jones, D.T. (2021). Alzheimer disease. *Nat Rev Dis Primers* 7, 33.

1189 Knouff, C., Hinsdale, M.E., Mezdour, H., Altenburg, M.K., Watanabe, M., Quarfordt, S.H.,  
1190 Sullivan, P.M., and Maeda, N. (1999). Apo E structure determines VLDL clearance and  
1191 atherosclerosis risk in mice. *The Journal of clinical investigation* 103, 1579-1586.

1192 Kunkle, B.W., Grenier-Boley, B., Sims, R., Bis, J.C., Damotte, V., Naj, A.C., Boland, A.,  
1193 Vronskaya, M., van der Lee, S.J., Amlie-Wolf, A., *et al.* (2019). Genetic meta-analysis of  
1194 diagnosed Alzheimer's disease identifies new risk loci and implicates Abeta, tau, immunity and  
1195 lipid processing. *Nature genetics* 51, 414-430.

1196 Kuznik, A., Bencina, M., Svajger, U., Jeras, M., Rozman, B., and Jerala, R. (2011). Mechanism  
1197 of endosomal TLR inhibition by antimalarial drugs and imidazoquinolines. *J Immunol* 186, 4794-  
1198 4804.

1199 Lane-Donovan, C., and Herz, J. (2017). ApoE, ApoE Receptors, and the Synapse in  
1200 Alzheimer's Disease. *Trends in endocrinology and metabolism: TEM* 28, 273-284.

1201 Lane-Donovan, C., Philips, G.T., and Herz, J. (2014). More than cholesterol transporters:  
1202 lipoprotein receptors in CNS function and neurodegeneration. *Neuron* 83, 771-787.

1203 Lane-Donovan, C., Philips, G.T., Wasser, C.R., Durakoglugil, M.S., Masiulis, I., Upadhaya, A.,  
1204 Pohlkamp, T., Coskun, C., Kotti, T., Steller, L., *et al.* (2015). Reelin protects against amyloid  
1205 beta toxicity in vivo. *Science signaling* 8, ra67.

1206 Lee, E.C., Yu, D., Martinez de Velasco, J., Tessarollo, L., Swing, D.A., Court, D.L., Jenkins,  
1207 N.A., and Copeland, N.G. (2001). A highly efficient Escherichia coli-based chromosome  
1208 engineering system adapted for recombinogenic targeting and subcloning of BAC DNA.  
1209 *Genomics* 73, 56-65.

1210 Lee, U., Choi, C., Ryu, S.H., Park, D., Lee, S.E., Kim, K., Kim, Y., and Chang, S. (2021a).  
1211 SCAMP5 plays a critical role in axonal trafficking and synaptic localization of NHE6 to adjust  
1212 quantal size at glutamatergic synapses. *Proceedings of the National Academy of Sciences of*  
1213 *the United States of America* 118.

1214 Lee, U., Ryu, S.H., and Chang, S. (2021b). SCAMP5 mediates activity-dependent enhancement  
1215 of NHE6 recruitment to synaptic vesicles during synaptic plasticity. *Mol Brain* 14, 47.

1216 Liao, F., Zhang, T.J., Jiang, H., Lefton, K.B., Robinson, G.O., Vassar, R., Sullivan, P.M., and  
1217 Holtzman, D.M. (2015). Murine versus human apolipoprotein E4: differential facilitation of and  
1218 co-localization in cerebral amyloid angiopathy and amyloid plaques in APP transgenic mouse  
1219 models. *Acta neuropathologica communications* 3, 70.

1220 Lucien, F., Pelletier, P.P., Lavoie, R.R., Lacroix, J.M., Roy, S., Parent, J.L., Arsenault, D.,  
1221 Harper, K., and Dubois, C.M. (2017). Hypoxia-induced mobilization of NHE6 to the plasma  
1222 membrane triggers endosome hyperacidification and chemoresistance. *Nature communications*  
1223 8, 15884.

1224 Ma, L., Ouyang, Q., Werthmann, G.C., Thompson, H.M., and Morrow, E.M. (2017). Live-cell  
1225 Microscopy and Fluorescence-based Measurement of Luminal pH in Intracellular Organelles.  
1226 *Front Cell Dev Biol* 5, 71.

1227 Madisen, L., Zwingman, T.A., Sunkin, S.M., Oh, S.W., Zariwala, H.A., Gu, H., Ng, L.L., Palmiter,  
1228 R.D., Hawrylycz, M.J., Jones, A.R., *et al.* (2010). A robust and high-throughput Cre reporting  
1229 and characterization system for the whole mouse brain. *Nature neuroscience* 13, 133-140.

1230 Meyer-Luehmann, M., Spires-Jones, T.L., Prada, C., Garcia-Alloza, M., de Calignon, A.,  
1231 Rozkalne, A., Koenigsknecht-Talboo, J., Holtzman, D.M., Bacskai, B.J., and Hyman, B.T.  
1232 (2008). Rapid appearance and local toxicity of amyloid-beta plaques in a mouse model of  
1233 Alzheimer's disease. *Nature* 451, 720-724.

1234 Minett, T., Classey, J., Matthews, F.E., Fahrenhold, M., Taga, M., Brayne, C., Ince, P.G., Nicoll,  
1235 J.A., Boche, D., and Mrc, C. (2016). Microglial immunophenotype in dementia with Alzheimer's  
1236 pathology. *J Neuroinflammation* 13, 135.

1237 Morrow, J.A., Hatters, D.M., Lu, B., Hochtl, P., Oberg, K.A., Rupp, B., and Weisgraber, K.H.  
1238 (2002). Apolipoprotein E4 forms a molten globule. A potential basis for its association with  
1239 disease. *The Journal of biological chemistry* 277, 50380-50385.

1240 Nakamura, N., Tanaka, S., Teko, Y., Mitsui, K., and Kanazawa, H. (2005). Four Na<sup>+</sup>/H<sup>+</sup>  
1241 exchanger isoforms are distributed to Golgi and post-Golgi compartments and are involved in  
1242 organelle pH regulation. *The Journal of biological chemistry* 280, 1561-1572.

1243 Naslavsky, N., and Caplan, S. (2018). The enigmatic endosome - sorting the ins and outs of  
1244 endocytic trafficking. *Journal of cell science* 131.

1245 Nixon, R.A. (2017). Amyloid precursor protein and endosomal-lysosomal dysfunction in  
1246 Alzheimer's disease: inseparable partners in a multifactorial disease. *FASEB journal : official  
1247 publication of the Federation of American Societies for Experimental Biology* 31, 2729-2743.

1248 Nuriel, T., Peng, K.Y., Ashok, A., Dillman, A.A., Figueroa, H.Y., Apuzzo, J., Ambat, J., Levy, E.,  
1249 Cookson, M.R., Mathews, P.M., *et al.* (2017). The Endosomal-Lysosomal Pathway Is  
1250 Dysregulated by APOE4 Expression in Vivo. *Frontiers in neuroscience* 11, 702.

1251 Ohgaki, R., Matsushita, M., Kanazawa, H., Ogihara, S., Hoekstra, D., and van Ijzendoorn, S.C.  
1252 (2010). The Na<sup>+</sup>/H<sup>+</sup> exchanger NHE6 in the endosomal recycling system is involved in the  
1253 development of apical bile canalicular surface domains in HepG2 cells. *Molecular biology of the  
1254 cell* 21, 1293-1304.

1255 Ordovas, J.M., Litwack-Klein, L., Wilson, P.W., Schaefer, M.M., and Schaefer, E.J. (1987).  
1256 Apolipoprotein E isoform phenotyping methodology and population frequency with identification  
1257 of apoE1 and apoE5 isoforms. *Journal of lipid research* 28, 371-380.

1258 Ouimet, M., Barrett, T.J., and Fisher, E.A. (2019). HDL and Reverse Cholesterol Transport. *Circ  
1259 Res* 124, 1505-1518.

1260 Ouyang, Q., Lizarraga, S.B., Schmidt, M., Yang, U., Gong, J., Ellisor, D., Kauer, J.A., and  
1261 Morrow, E.M. (2013). Christianson syndrome protein NHE6 modulates TrkB endosomal  
1262 signaling required for neuronal circuit development. *Neuron* 80, 97-112.

1263 Panza, F., Solfrizzi, V., Torres, F., Mastroianni, F., Colacicco, A.M., Basile, A.M., Capurso, C.,  
1264 D'Introno, A., Del Parigi, A., and Capurso, A. (2000). Apolipoprotein E in Southern Italy:  
1265 protective effect of epsilon 2 allele in early- and late-onset sporadic Alzheimer's disease.  
1266 *Neuroscience letters* 292, 79-82.

1267 Parhizkar, S., Arzberger, T., Brendel, M., Kleinberger, G., Deussing, M., Focke, C., Nuscher, B.,  
1268 Xiong, M., Ghasemigharagoz, A., Katzmarski, N., *et al.* (2019). Loss of TREM2 function  
1269 increases amyloid seeding but reduces plaque-associated ApoE. *Nature neuroscience* 22, 191-  
1270 204.

1271 Pensalfini, A., Kim, S., Subbanna, S., Bleiwas, C., Goulbourne, C.N., Stavrides, P.H., Jiang, Y.,  
1272 Lee, J.H., Darji, S., Pawlik, M., *et al.* (2020). Endosomal Dysfunction Induced by Directly  
1273 Overactivating Rab5 Recapitulates Prodromal and Neurodegenerative Features of Alzheimer's  
1274 Disease. *Cell Rep* 33, 108420.

1275 Pohlkamp, T., Wasser, C.R., and Herz, J. (2017). Functional Roles of the Interaction of APP and  
1276 Lipoprotein Receptors. *Frontiers in molecular neuroscience* 10, 54.

1277 Prasad, H., and Rao, R. (2015). The Na<sup>+</sup>/H<sup>+</sup> exchanger NHE6 modulates endosomal pH to  
1278 control processing of amyloid precursor protein in a cell culture model of Alzheimer disease. *The  
1279 Journal of biological chemistry* 290, 5311-5327.

1280 Prasad, H., and Rao, R. (2018). Amyloid clearance defect in ApoE4 astrocytes is reversed by  
1281 epigenetic correction of endosomal pH. *Proceedings of the National Academy of Sciences*,  
1282 201801612.

1283 Rawat, V., Wang, S., Sima, J., Bar, R., Liraz, O., Gundimeda, U., Parekh, T., Chan, J.,  
1284 Johansson, J.O., Tang, C., *et al.* (2019). ApoE4 Alters ABCA1 Membrane Trafficking in  
1285 Astrocytes. *The Journal of neuroscience : the official journal of the Society for Neuroscience* 39,  
1286 9611-9622.

1287 Reiman, E.M., Arboleda-Velasquez, J.F., Quiroz, Y.T., Huentelman, M.J., Beach, T.G., Caselli,  
1288 R.J., Chen, Y., Su, Y., Myers, A.J., Hardy, J., *et al.* (2020). Exceptionally low likelihood of  
1289 Alzheimer's dementia in APOE2 homozygotes from a 5,000-person neuropathological study.  
1290 *Nature communications* 11, 667.

1291 Roses, A.D. (1994). Apolipoprotein E affects the rate of Alzheimer disease expression: beta-  
1292 amyloid burden is a secondary consequence dependent on APOE genotype and duration of  
1293 disease. *Journal of neuropathology and experimental neurology* 53, 429-437.

1294 Rudenko, G., Henry, L., Henderson, K., Ichtchenko, K., Brown, M.S., Goldstein, J.L., and  
1295 Deisenhofer, J. (2002). Structure of the LDL receptor extracellular domain at endosomal pH.  
1296 *Science* 298, 2353-2358.

1297 Saito, T., Matsuba, Y., Mihira, N., Takano, J., Nilsson, P., Itohara, S., Iwata, N., and Saido, T.C.  
1298 (2014). Single App knock-in mouse models of Alzheimer's disease. *Nature neuroscience* 17,  
1299 661-663.

1300 Sando, S.B., Melquist, S., Cannon, A., Hutton, M.L., Sletvold, O., Saltvedt, I., White, L.R.,  
1301 Lydersen, S., and Aasly, J.O. (2008). APOE epsilon 4 lowers age at onset and is a high risk  
1302 factor for Alzheimer's disease; a case control study from central Norway. *BMC neurology* 8, 9.

1303 Sarlus, H., and Heneka, M.T. (2017). Microglia in Alzheimer's disease. *The Journal of clinical*  
1304 *investigation* 127, 3240-3249.

1305 Schmid, S.L. (2017). Reciprocal regulation of signaling and endocytosis: Implications for the  
1306 evolving cancer cell. *The Journal of cell biology* 216, 2623-2632.

1307 Serrano-Pozo, A., Muzikansky, A., Gomez-Isla, T., Growdon, J.H., Betensky, R.A., Frosch,  
1308 M.P., and Hyman, B.T. (2013). Differential relationships of reactive astrocytes and microglia to  
1309 fibrillar amyloid deposits in Alzheimer disease. *Journal of neuropathology and experimental*  
1310 *neurology* 72, 462-471.

1311 Sevigny, J., Chiao, P., Bussiere, T., Weinreb, P.H., Williams, L., Maier, M., Dunstan, R.,  
1312 Salloway, S., Chen, T., Ling, Y., *et al.* (2016). The antibody aducanumab reduces Abeta  
1313 plaques in Alzheimer's disease. *Nature* 537, 50-56.

1314 Shi, Y., Andhey, P.S., Ising, C., Wang, K., Snipes, L.L., Boyer, K., Lawson, S., Yamada, K., Qin,  
1315 W., Manis, M., *et al.* (2021). Overexpressing low-density lipoprotein receptor reduces tau-  
1316 associated neurodegeneration in relation to apoE-linked mechanisms. *Neuron*.

1317 Shimizu, H., Tosaki, A., Kaneko, K., Hisano, T., Sakurai, T., and Nukina, N. (2008). Crystal  
1318 structure of an active form of BACE1, an enzyme responsible for amyloid beta protein  
1319 production. *Molecular and cellular biology* 28, 3663-3671.

1320 Shore, V.G., and Shore, B. (1973). Heterogeneity of human plasma very low density  
1321 lipoproteins. Separation of species differing in protein components. *Biochemistry* 12, 502-507.

1322 Sinclair, R.A., Burns, J., and Dunnill, M.S. (1981). Immunoperoxidase staining of formalin-fixed,  
1323 paraffin-embedded, human renal biopsies with a comparison of the peroxidase-antiperoxidase  
1324 (PAP) and indirect methods. *Journal of clinical pathology* 34, 859-865.

1325 Small, S.A., Simoes-Spassov, S., Mayeux, R., and Petsko, G.A. (2017). Endosomal Traffic  
1326 Jams Represent a Pathogenic Hub and Therapeutic Target in Alzheimer's Disease. *Trends*  
1327 *Neurosci* 40, 592-602.

1328 Stawicki, T.M., Owens, K.N., Linbo, T., Reinhart, K.E., Rubel, E.W., and Raible, D.W. (2014).  
1329 The zebrafish merovingian mutant reveals a role for pH regulation in hair cell toxicity and  
1330 function. *Dis Model Mech* 7, 847-856.

1331 Stromme, P., Dobrenis, K., Sillitoe, R.V., Gulinello, M., Ali, N.F., Davidson, C., Micsenyi, M.C.,  
1332 Stephney, G., Ellevog, L., Klungland, A., *et al.* (2011). X-linked Angelman-like syndrome caused  
1333 by Slc9a6 knockout in mice exhibits evidence of endosomal-lysosomal dysfunction. *Brain : a*  
1334 *journal of neurology* 134, 3369-3383.

1335 Sullivan, P.M., Mezdour, H., Aratani, Y., Knouff, C., Najib, J., Reddick, R.L., Quarfordt, S.H., and  
1336 Maeda, N. (1997). Targeted replacement of the mouse apolipoprotein E gene with the common  
1337 human APOE3 allele enhances diet-induced hypercholesterolemia and atherosclerosis. *The*  
1338 *Journal of biological chemistry* 272, 17972-17980.

1339 Tallquist, M.D., and Soriano, P. (2000). Epiblast-restricted Cre expression in MORE mice: a tool  
1340 to distinguish embryonic vs. extra-embryonic gene function. *Genesis* 26, 113-115.

1341 Trommsdorff, M., Gotthardt, M., Hiesberger, T., Shelton, J., Stockinger, W., Nimpf, J., Hammer,  
1342 R.E., Richardson, J.A., and Herz, J. (1999). Reeler/Disabled-like disruption of neuronal  
1343 migration in knockout mice lacking the VLDL receptor and ApoE receptor 2. *Cell* 97, 689-701.

1344 Van Acker, Z.P., Bretou, M., and Annaert, W. (2019). Endo-lysosomal dysregulations and late-  
1345 onset Alzheimer's disease: impact of genetic risk factors. *Molecular neurodegeneration* 14, 20.

1346 Vassar, R., Bennett, B.D., Babu-Khan, S., Kahn, S., Mendiaz, E.A., Denis, P., Teplow, D.B.,  
1347 Ross, S., Amarante, P., Loeloff, R., *et al.* (1999). Beta-secretase cleavage of Alzheimer's  
1348 amyloid precursor protein by the transmembrane aspartic protease BACE. *Science* 286, 735-  
1349 741.

1350 Verheijen, J., and Sleegers, K. (2018). Understanding Alzheimer Disease at the Interface  
1351 between Genetics and Transcriptomics. *Trends Genet* 34, 434-447.

1352 Wahrle, S.E., Jiang, H., Parsadanian, M., Hartman, R.E., Bales, K.R., Paul, S.M., and Holtzman,  
1353 D.M. (2005). Deletion of Abca1 increases Abeta deposition in the PDAPP transgenic mouse  
1354 model of Alzheimer disease. *The Journal of biological chemistry* 280, 43236-43242.

1355 Wahrle, S.E., Jiang, H., Parsadanian, M., Kim, J., Li, A., Knoten, A., Jain, S., Hirsch-  
1356 Reinshagen, V., Wellington, C.L., Bales, K.R., *et al.* (2008). Overexpression of ABCA1 reduces  
1357 amyloid deposition in the PDAPP mouse model of Alzheimer disease. *The Journal of clinical*  
1358 *investigation* 118, 671-682.

- 1359 Wahrle, S.E., Jiang, H., Parsadanian, M., Legleiter, J., Han, X., Fryer, J.D., Kowalewski, T., and  
1360 Holtzman, D.M. (2004). ABCA1 is required for normal central nervous system ApoE levels and  
1361 for lipidation of astrocyte-secreted apoE. *The Journal of biological chemistry* 279, 40987-40993.
- 1362 Wang, M., Jing, T., Wang, X., and Yao, D. (2018). Beta-secretase/BACE1 promotes APP  
1363 endocytosis and processing in the endosomes and on cell membrane. *Neuroscience letters* 685,  
1364 63-67.
- 1365 Warnick, G.R., Mayfield, C., Albers, J.J., and Hazzard, W.R. (1979). Gel isoelectric focusing  
1366 method for specific diagnosis of familial hyperlipoproteinemia type 3. *Clinical chemistry* 25, 279-  
1367 284.
- 1368 Weeber, E.J., Beffert, U., Jones, C., Christian, J.M., Forster, E., Sweatt, J.D., and Herz, J.  
1369 (2002). Reelin and ApoE receptors cooperate to enhance hippocampal synaptic plasticity and  
1370 learning. *The Journal of biological chemistry* 277, 39944-39952.
- 1371 West, H.L., Rebeck, G.W., and Hyman, B.T. (1994). Frequency of the apolipoprotein E epsilon 2  
1372 allele is diminished in sporadic Alzheimer disease. *Neuroscience letters* 175, 46-48.
- 1373 Wintersteiner, O., and Abramson, H.A. (1933). The isoelectric point of insulin: Electrical  
1374 properties of adsorbed and crystalline insulin. *J Biol Chem* 99, 741-753.
- 1375 Wozniacka, A., Lesiak, A., Narbutt, J., McCauliffe, D.P., and Sysa-Jedrzejowska, A. (2006).  
1376 Chloroquine treatment influences proinflammatory cytokine levels in systemic lupus  
1377 erythematosus patients. *Lupus* 15, 268-275.
- 1378 Xian, X., Pohlkamp, T., Durakoglugil, M.S., Wong, C.H., Beck, J.K., Lane-Donovan, C., Plattner,  
1379 F., and Herz, J. (2018). Reversal of ApoE4-induced recycling block as a novel prevention  
1380 approach for Alzheimer's disease. *eLife* 7.
- 1381 Xinhan, L., Matsushita, M., Numaza, M., Taguchi, A., Mitsui, K., and Kanazawa, H. (2011).  
1382 Na<sup>+</sup>/H<sup>+</sup> exchanger isoform 6 (NHE6/SLC9A6) is involved in clathrin-dependent endocytosis of  
1383 transferrin. *American journal of physiology Cell physiology* 301, C1431-1444.
- 1384 Xu, M., Ouyang, Q., Gong, J., Pescosolido, M.F., Pruett, B.S., Mishra, S., Schmidt, M., Jones,  
1385 R.N., Gamsiz Uzun, E.D., Lizarraga, S.B., *et al.* (2017). Mixed Neurodevelopmental and  
1386 Neurodegenerative Pathology in Nhe6-Null Mouse Model of Christianson Syndrome. *eNeuro* 4.
- 1387 Yamamoto, T., Chen, H.C., Guigard, E., Kay, C.M., and Ryan, R.O. (2008). Molecular studies of  
1388 pH-dependent ligand interactions with the low-density lipoprotein receptor. *Biochemistry* 47,  
1389 11647-11652.
- 1390 Yamazaki, Y., Zhao, N., Caulfield, T.R., Liu, C.C., and Bu, G. (2019). Apolipoprotein E and  
1391 Alzheimer disease: pathobiology and targeting strategies. *Nature reviews Neurology* 15, 501-  
1392 518.
- 1393 Yang, H., Kozicky, L., Saferali, A., Fung, S.Y., Afacan, N., Cai, B., Falsafi, R., Gill, E., Liu, M.,  
1394 Kollmann, T.R., *et al.* (2016). Endosomal pH modulation by peptide-gold nanoparticle hybrids  
1395 enables potent anti-inflammatory activity in phagocytic immune cells. *Biomaterials* 111, 90-102.
- 1396 Yanuck, S.F. (2019). Microglial Phagocytosis of Neurons: Diminishing Neuronal Loss in  
1397 Traumatic, Infectious, Inflammatory, and Autoimmune CNS Disorders. *Front Psychiatry* 10, 712.

1398 Zhang, Y., Chen, K., Sloan, S.A., Bennett, M.L., Scholze, A.R., O'Keefe, S., Phatnani, H.P.,  
1399 Guarnieri, P., Caneda, C., Ruderisch, N., *et al.* (2014). An RNA-sequencing transcriptome and  
1400 splicing database of glia, neurons, and vascular cells of the cerebral cortex. *The Journal of*  
1401 *neuroscience : the official journal of the Society for Neuroscience* *34*, 11929-11947.

1402 Zhong, L., Xu, Y., Zhuo, R., Wang, T., Wang, K., Huang, R., Wang, D., Gao, Y., Zhu, Y., Sheng,  
1403 X., *et al.* (2019). Soluble TREM2 ameliorates pathological phenotypes by modulating microglial  
1404 functions in an Alzheimer's disease model. *Nature communications* *10*, 1365.

1405 Ziegler-Waldkirch, S., and Meyer-Luehmann, M. (2018). The Role of Glial Cells and Synapse  
1406 Loss in Mouse Models of Alzheimer's Disease. *Frontiers in cellular neuroscience* *12*, 473.

1407

1 **Key Resources Table**

Reagent type (species) or resource	Designation	Source or reference	Identifiers	Additional information
strain, strain background ( <i>Mus musculus</i> )	Mouse/ <i>Slc9a6</i> <sup>fl</sup>	This study		Refer to Methods section for detailed description of mouse model production.
strain, strain background ( <i>Mus musculus</i> )	Mouse/ <i>Slc9a6</i> <sup>-</sup>	This study		Refer to Methods section for detailed description of mouse model production.
strain, strain background ( <i>Mus musculus</i> )	Mouse/ <i>ApoE</i> <sup>APOE3</sup> <sub>E3</sub>	Sullivan et al., 1997	IMSR_TAC:2542	<i>ApoE</i> <sup>APOE3</sup>
strain, strain background ( <i>Mus musculus</i> )	Mouse/ <i>ApoE</i> <sup>APOE4</sup> <sub>E4</sub>	Knouff et al., 1999	IMSR_TAC:3518	<i>ApoE</i> <sup>APOE4</sup>
strain, strain background ( <i>Mus musculus</i> )	Mouse/B6.Cg-Gt(ROSA)26Sor <sup>tm9</sup> (CAG-tdTomato)Hze/J	The Jackson Laboratory Madisen et al., 2010	JAX #007909	<i>ROSA</i> <sup>flxedStop-tdTomato</sup>
strain, strain background ( <i>Mus musculus</i> )	Mouse/CAG-cre/ <i>Esr1</i> <sup>5Amc</sup> /J	The Jackson Laboratory Hayashi et al., 2002	JAX #004682	<i>CAG-Cre</i> <sup>ERT2</sup>
strain, strain background ( <i>Mus musculus</i> )	Mouse/B6.129S4-Meox2 <sup>tm1</sup> (cre)Sor/J	The Jackson Laboratory Tallquist and Soriano 2000	JAX 003755	<i>Meox-Cre</i>
strain, strain background ( <i>Mus musculus</i> )	<i>App</i> <sup>NL-F</sup>	Saito et al., 2014		<i>App</i> <sup>NL-F</sup>
strain, strain background ( <i>Mus musculus</i> )	Tg2576	Charles River Hsiao et al., 1996	Charles River Tg2576	Tg2576, <i>APP</i> <sup>Swe</sup>
strain, strain background ( <i>Rattus</i> )	SD rat	Charles River	SC:400	

<i>norvegicus</i> )				
cell line ( <i>Homo sapiens</i> )	HEK293	Thermo Fisher	R70507, RRID:CVCL_0045	
cell line ( <i>Homo sapiens</i> )	HEK293-T	ATCC	CRL-3216	
cell line ( <i>Mus musculus</i> )	Neuro-2a	ATCC	CCL-131	
cell line ( <i>Mus musculus</i> )	NHE6-KO ( <i>Slc9a6</i> <sup>-</sup> ) mouse embryonic fibroblasts (MEFs)	This study		Refer to Methods section for detailed description of MEF production.
cell line ( <i>Mus musculus</i> )	<i>Slc9a6</i> <sup>+</sup> MEFs ( <i>Slc9a6</i> <sup>-</sup> littermate)	This study		Refer to Methods section for detailed description of MEF production.
antibody	anti-A $\beta$ (clone 6E10) (Mouse monoclonal)	Covance	SIG-39320 RRID:AB_662798	WB and IHC (1:1000)
antibody	anti-A $\beta$ (clone 4G8) (Mouse monoclonal)	Covance	SIG-39220 RRID:AB_10175152	IHC (1:1000)
antibody	anti-phosphotyrosine (clone 4G10) (Mouse monoclonal)	EMD Millipore	Millipore Cat# 05-321, RRID:AB_309678	WB (1:1000)
antibody	anti-Apoer2 (Rabbit polyclonal)	Herz Lab, #2561, Trommsdorff et al., 1999		WB (1:1000)
antibody	anti- $\beta$ -Actin (Rabbit polyclonal)	Abcam	Ab8227, RRID:AB_2305186	WB (1:3000)
antibody	Anti-Calbindin D-28k (Mouse monoclonal)	Swant	Swant Cat# 300, RRID:AB_10000347	IHC (1:1000)

antibody	Anti-GFAP (Rabbit polyclonal)	Abcam	Abcam Cat# ab7260, RRID:AB_30580 8	IHC (1:2000)
antibody	Anti-GluA1 (Rabbit polyclonal)	Abcam	ab31232, RRID:AB_21134 47	WB (1:1000)
antibody	Anti-GluA2/3 (Rabbit polyclonal)	EMD Millipore	07-598, RRID:AB_31074 1	WB (1:1000)
antibody	Anti-GluN2B (Rabbit polyclonal)	Cell Signaling Technology	4207S, RRID:AB_12642 23	WB (1:1000)
antibody	Anti-Iba1 (Rabbit polyclonal)	Wako	019-19741, RRID:AB_83950 4	IHC (1:1000)
antibody	Anti-NHE6 (C-terminus) (Rabbit polyclonal)	Herz Lab, Xian et al., 2018		WB (1:1000)
antibody	Anti-mouse-IgG AF594 (Goat polyclonal)	Thermo Fisher	A-11032, RRID:AB_25340 91	IHC (1:500)
antibody	Anti-rabbit-IgG AF488 (Goat polyclonal)	Thermo Fisher	A-11034, RRID:AB_25762 17	IHC (1:500)
Commercial assay or kit	Anti-mouse-IgG staining kit	Vector	MP-7602, RRID:AB_23365 32	
commercial assay or kit	Anti-rabbit-IgG staining kit	Vector	MP-7601, RRID:AB_23365 33	
chemical compound, drug	Antigen retrieval citrate buffer	BioGenex, Cat	HK086-9K	
chemical compound, drug	B-27 Supplement	Thermo Fisher	17504044	

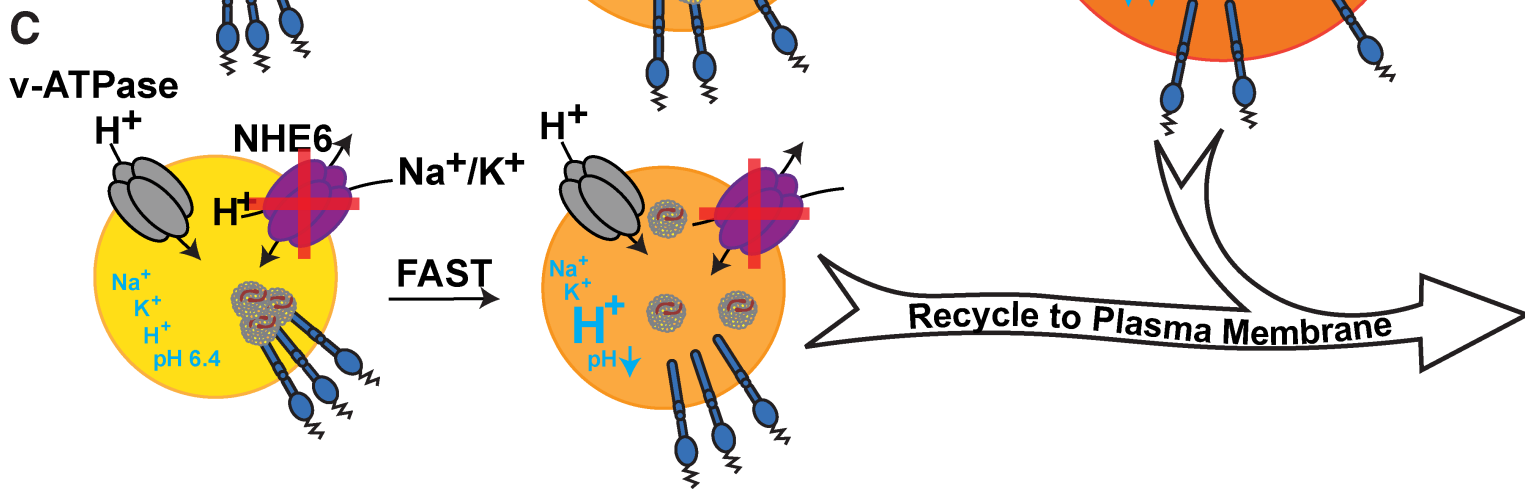
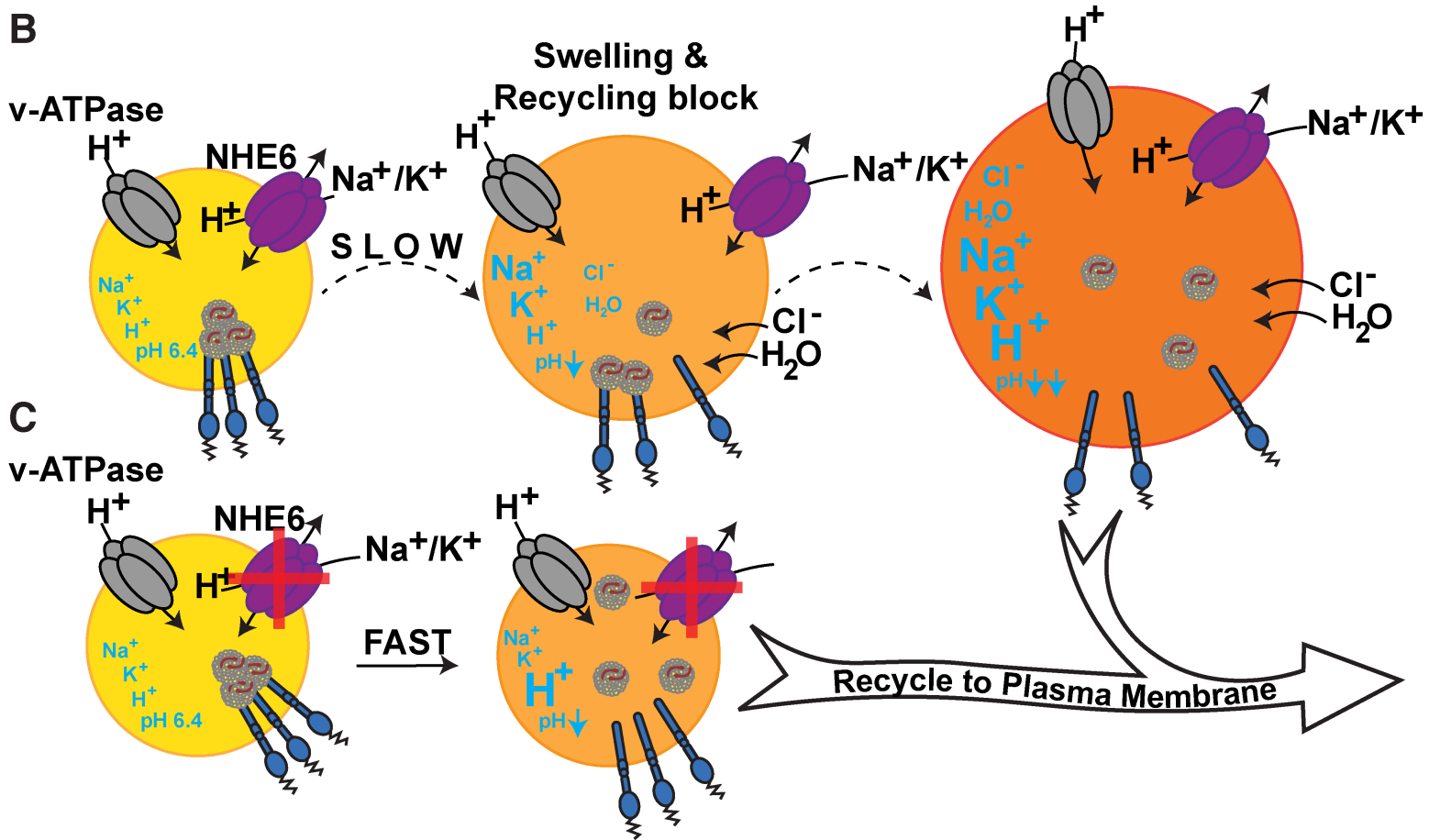
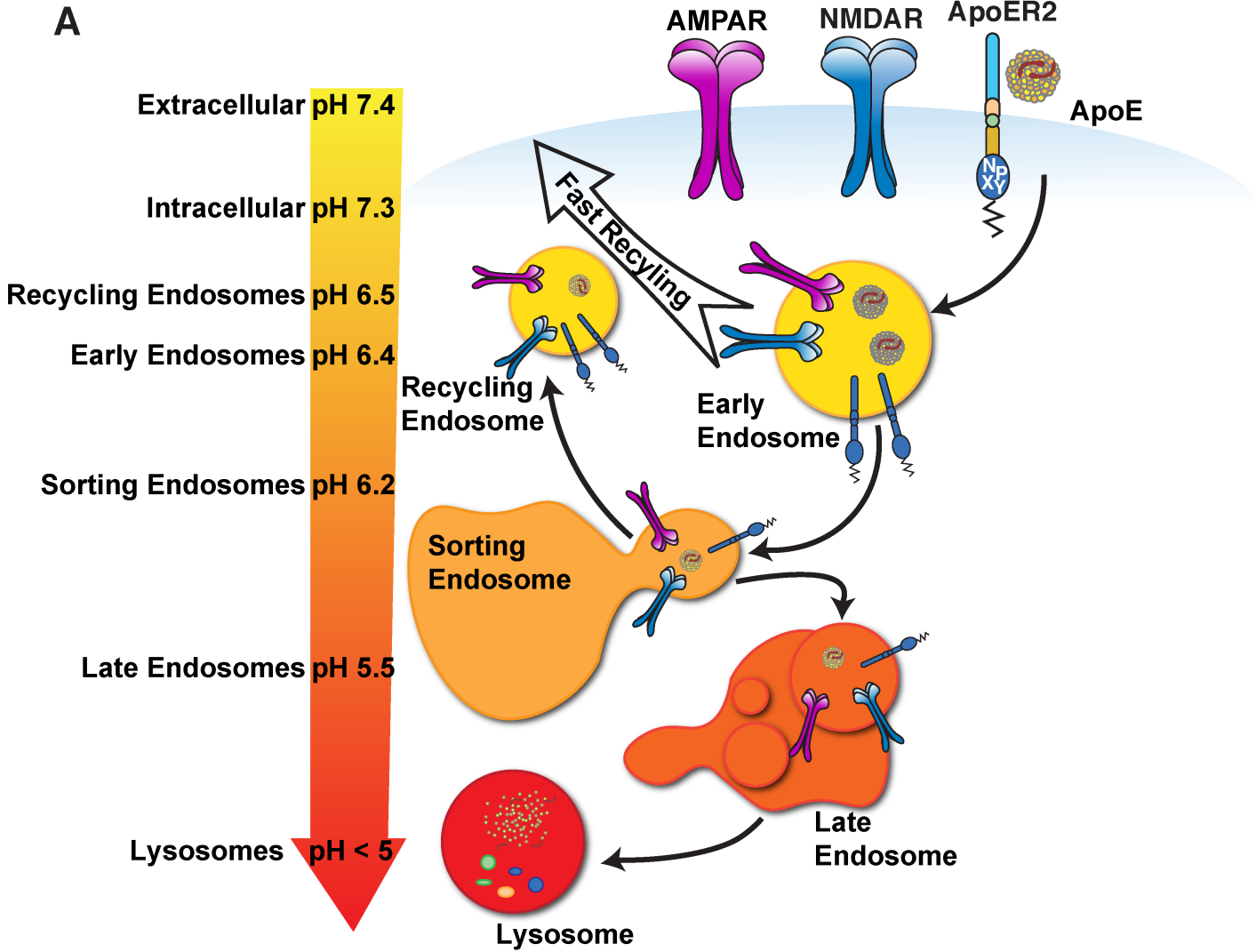
	(50X), serum free			
chemical compound, drug	Cytoseal 60	Thermo Fisher	8310	
chemical compound, drug	DMEM	Sigma-Aldrich	D6046	
chemical compound, drug	FuGENE	Promega	E2311	
chemical compound, drug	HBSS (1X)	Gibco	14175	
chemical compound, drug	L-Glutamic acid (Glutamate)	Sigma-Aldrich	G1251	
chemical compound, drug	$\gamma$ -secretase inhibitor L-685458	Tocris Bioscience	2627	
chemical compound, drug	Penicillin-Streptomycin Solution, 100X	Corning	30-002-CI	
chemical compound, drug	Neurobasal Medium (1X) Liquid without Phenol Red	Thermo Fisher	12348017	
chemical compound, drug	NeutrAvidin Agarose	Thermo Fisher	29201	
chemical compound, drug	Nonidet P-40 Alternative	EMD Millipore	492016	
chemical compound, drug	32% Paraformaldehyde AQ solution	Fisher Scientific	15714S	
chemical compound, drug	PBS (1X)	Sigma-Aldrich	D8537	
chemical compound, drug	Penicillin-Streptomycin	Corning	30-002-CI	
chemical compound, drug	Phosphatase Inhibitor	Thermo Fisher	78420	

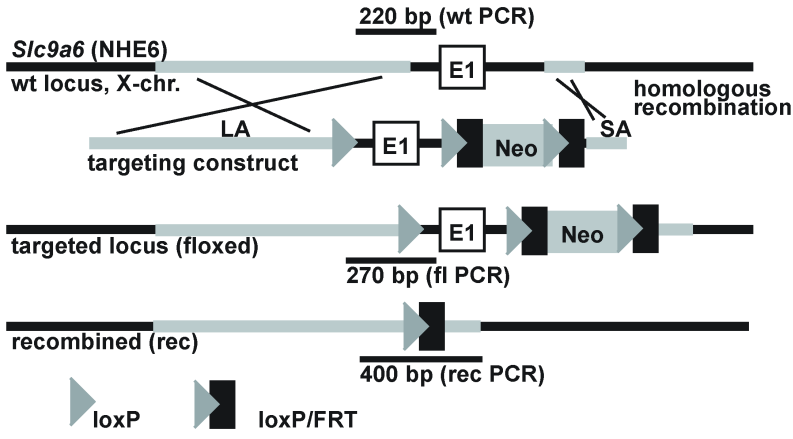
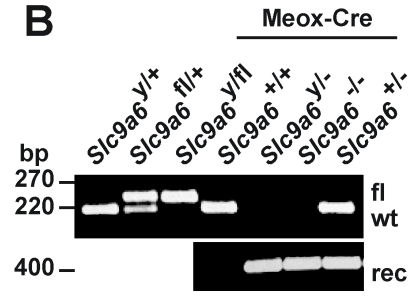
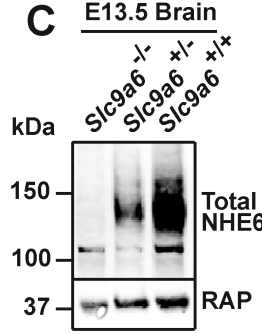
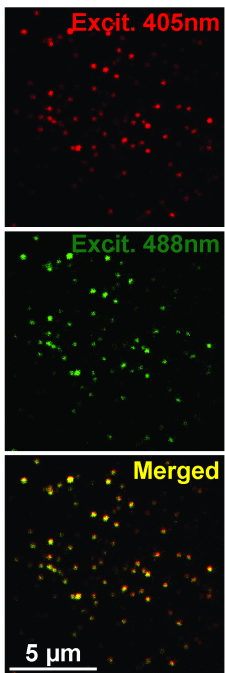
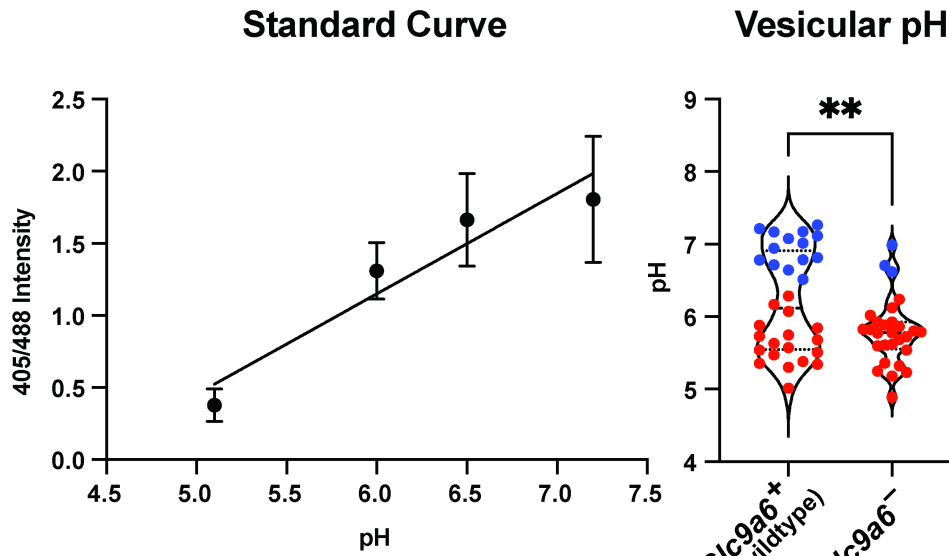
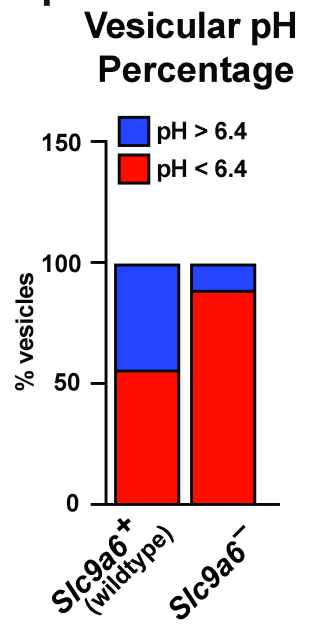
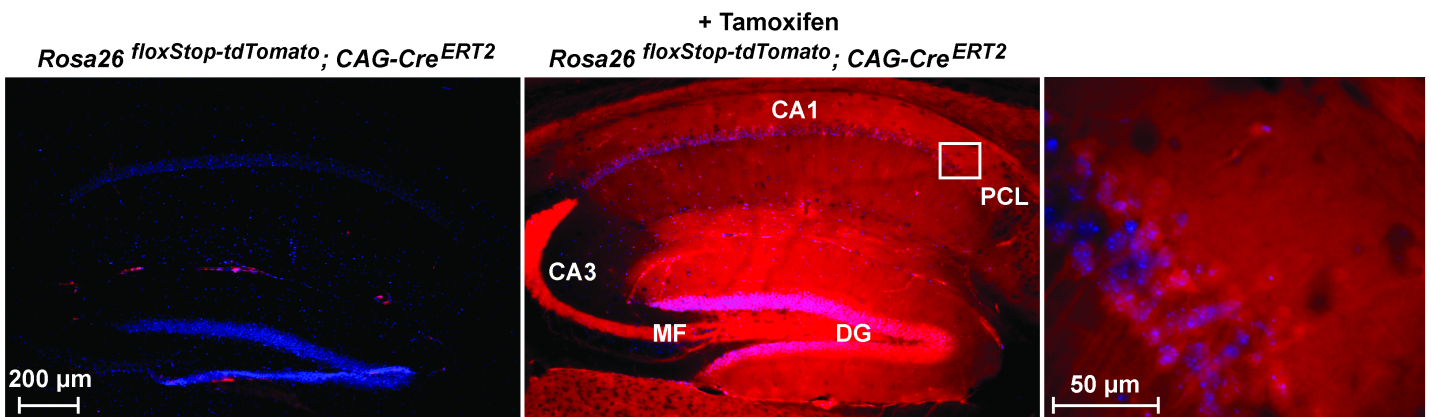
	Cocktail			
chemical compound, drug	Poly-D-Lysine	Sigma-Aldrich	A-003-M	
chemical compound, drug	Protein A-Sepharose 4B	Thermo Fisher	101042	
chemical compound, drug	Proteinase Inhibitor Cocktail	Sigma-Aldrich	P8340	
chemical compound, drug	Sulfo-NHS-SS-biotin	Pierce	21331	
chemical compound, drug	Triton X-100	Sigma-Aldrich	CAS9002-93-1	
chemical compound, drug	Tween 20	Sigma	P1379	
other	Vectashield with DAPI	Vector Labs	H-1200	(DAPI 1.5 µg/mL)
transfected construct ( <i>Mus musculus</i> )	pCrl, Reelin expression vector	(D'Arcangelo et al., 1997)	N/A	
transfected construct ( <i>Homo sapiens</i> )	pcDNA3.1-ApoE3	Chen et al., 2010	N/A	progenitor pcDNA3.1-Zeo
transfected construct ( <i>Homo sapiens</i> )	pcDNA3.1-ApoE4	Chen et al., 2010	N/A	progenitor pcDNA3.1-Zeo
transfected construct ( <i>Mus musculus</i> )	pLKO.1 scramble shRNA	Xian et al., 2018	N/A	
transfected construct ( <i>Mus musculus</i> )	pLKO.1 shNHE6	Open Biosystem	TRCN0000068828	Refers to shNHE6-a in Xian et al., 2018
transfected construct ( <i>Mus musculus</i> )	psPAX2	Addgene	12260	Plasmid was a gift from Didier Trono
transfected	pMD2.G	Addgene	12259	Plasmid was a gift from Didier

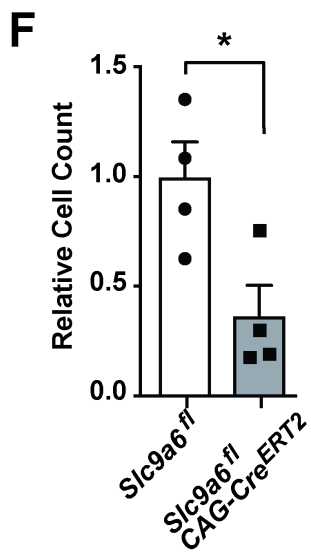
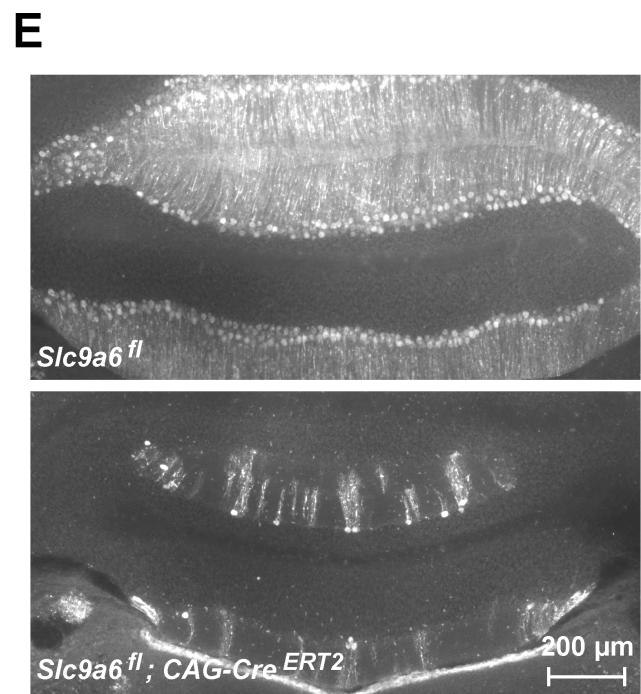
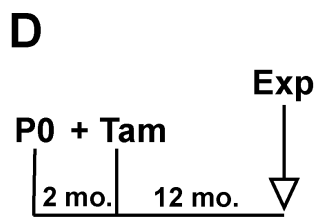
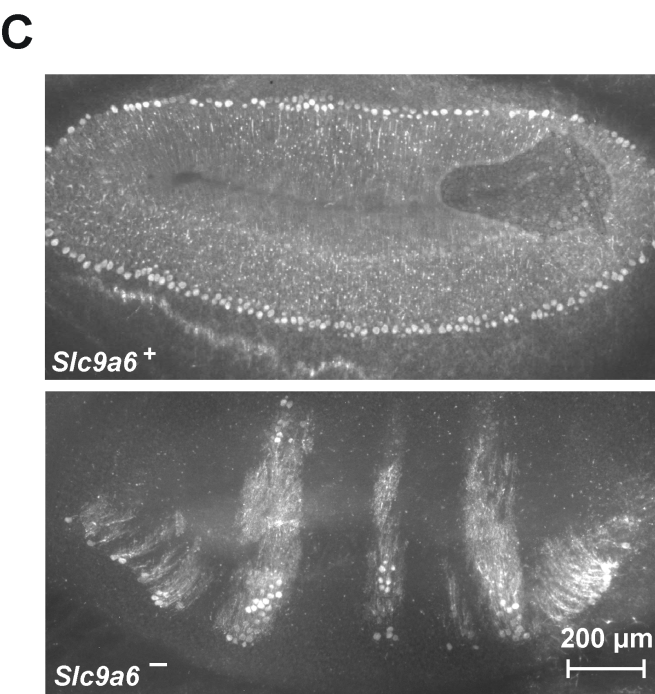
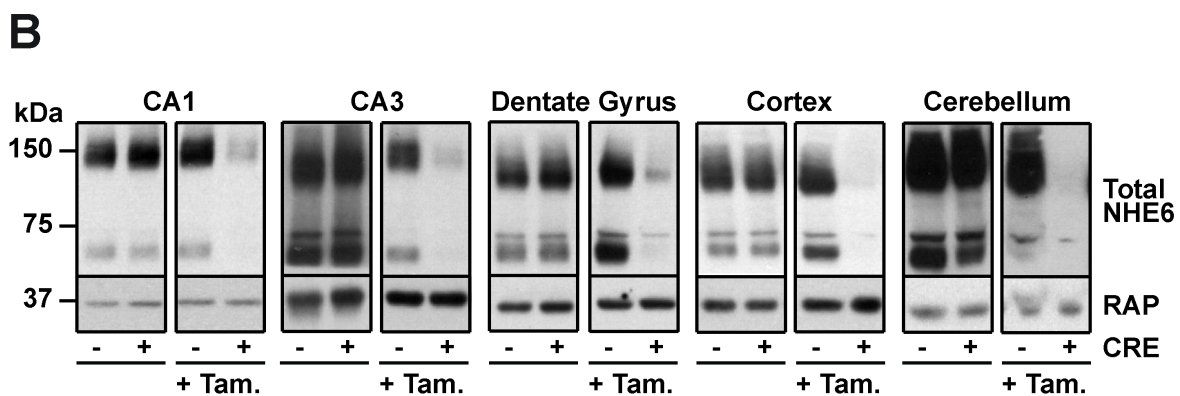
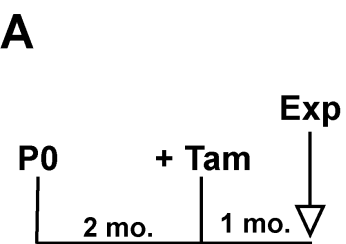
construct ( <i>Mus musculus</i> )				Trono
transfected construct ( <i>Mus musculus</i> )	pJB-NHE6 targeting vector	This study	N/A	Refer to Methods section for detailed description.
Recombinant DNA reagent	pJB1 (plasmid)	Braybrooke et al., 2000	N/A	
Recombinant DNA reagent	pCR4-TOPO (plasmid)	Thermofisher	K457502	
Recombinant DNA reagent	pLVCMVfull (plasmid)	Xian et al., 2018	N/A	
Recombinant DNA reagent	pME (plasmid)	Stawicki et al., 2014	Addgene #73794	Plasmid was a gift from David Raible
Recombinant DNA reagent	pLVCMV Vamp3-pHluorin2 (plasmid)	This study	N/A	Refer to Methods section for detailed description.
Recombinant DNA reagent	BAC containing murine NHE6 sequence (Bacterial artificial chromosome)	BACPAC Resources Center	RP23 364F14	
software, algorithm	Adobe Creative Cloud	Adobe	RRID:SCR_010279	
software, algorithm	GraphPad Prism 7.0	GraphPad Software	RRID:SCR_002798	
software, algorithm	Fiji/ImageJ	NIH	RRID:SCR_002285	
software, algorithm	LabView7.0	National Instruments	RRID:SCR_014325	
software, algorithm	NDP.view2	Hamamatsu Photonics		
software, algorithm	Odyssey Imaging System	LI-COR	RRID:SCR_014579	

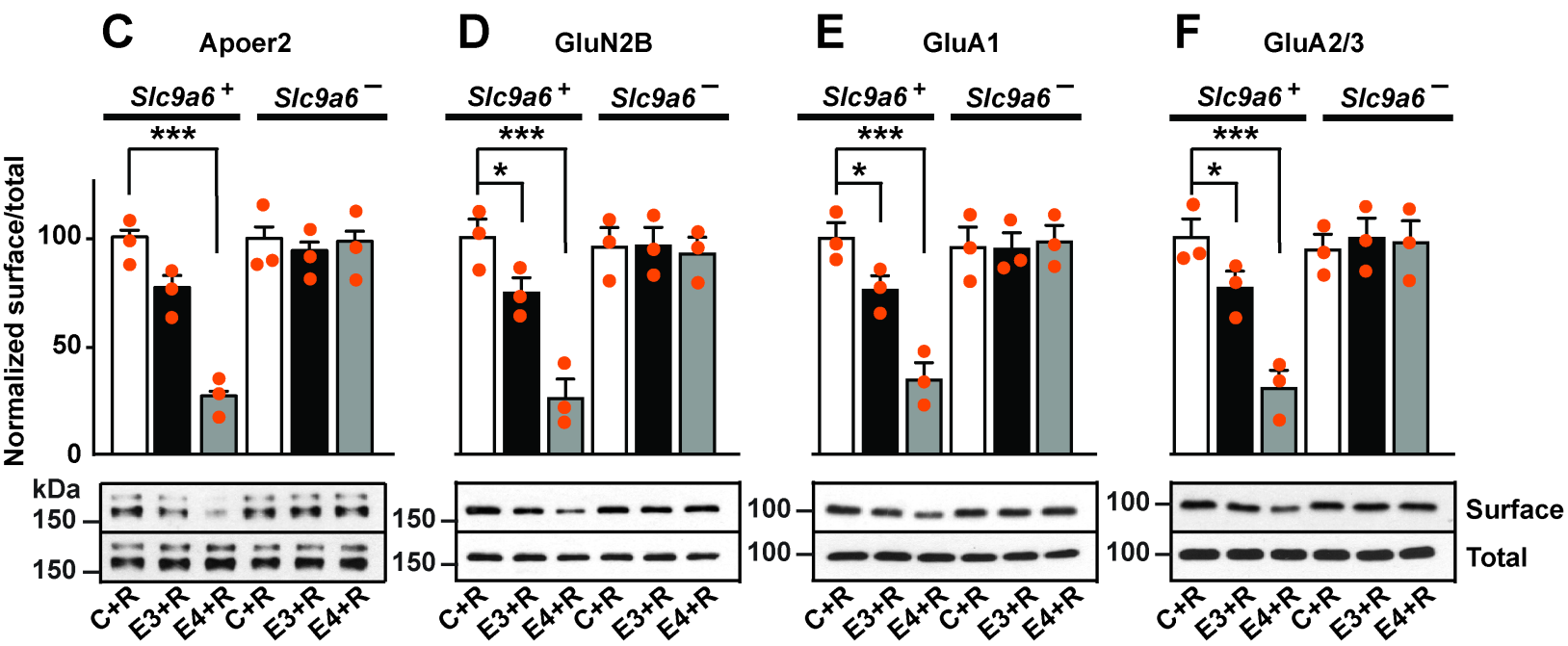
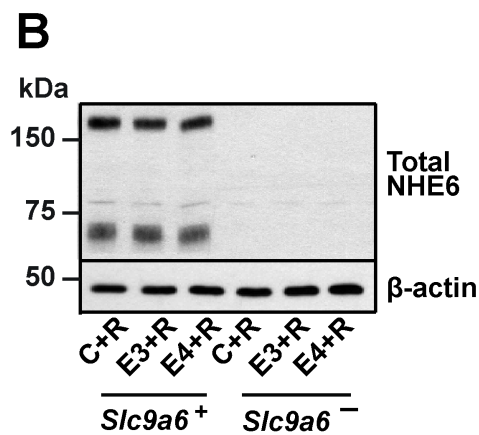
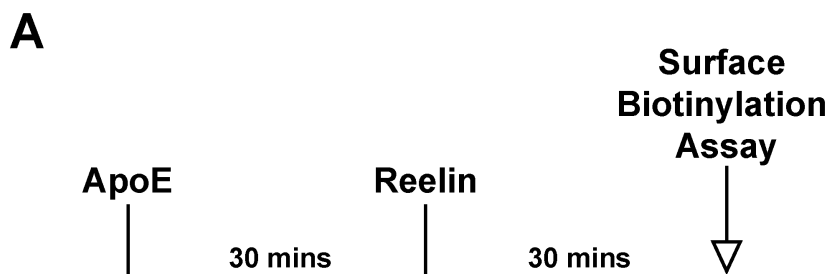
software, algorithm	Clustal Omega	EMBL-EBI	RRID:SCR_0015 91	
software, algorithm	Leica TCS SPE	Leica	RRID:SCR_0021 40	
Sequence-based reagent	SA forward	IDT		GGATCCGTGTGTGTGTTGG GGGAGGGA
Sequence-based reagent	SA reverse	Integrated DNA Technology		CTCGAGCTCACAATCAGCCC TTTAAATATGCC
Sequence-based reagent	GAP repair US forward	Integrated DNA Technology		AAGCTTGC GGCCGCTTCAAT TTCTGTCCTTGCTACTG
Sequence-based reagent	GAP repair US reverse	Integrated DNA Technology		AGATCTCAAGAAAGTTAGCT AGAAGTGTGTC
Sequence-based reagent	GAP repair DS forward	Integrated DNA Technology		AGATCTGTAGAGGATGTGG GAAAGAGAG
Sequence-based reagent	GAP repair DS reverse	Integrated DNA Technology		GTCGACGCGCCGACACAC ACAGATAAATAACCTCAAAA G
Sequence-based reagent	5' flanking 1 <sup>st</sup> LoxP fragment forward	Integrated DNA Technology		GCTTCTCTCGAGCAAGAGTC AAC
Sequence-based reagent	5' flanking 1 <sup>st</sup> LoxP fragment reverse	Integrated DNA Technology		GATATCAGCAGGTACCACCA AGATCTCAACCTTATTGTCC TATATGCACAAAC
Sequence-based reagent	3' flanking 1 <sup>st</sup> LoxP fragment forward	Integrated DNA Technology		GTCTTGTGGTACCTGATGA AATGGACTACCTCCACTTG
Sequence-based reagent	3' flanking 1 <sup>st</sup> LoxP fragment reverse	Integrated DNA Technology		ATCGATCTTCATAACCCATC TGGATA
Sequence-based reagent	LoxP Oligo forward	Integrated DNA Technology		GATCTGCTCAGCATAACTTC GTATAGCATAATTATACGA AGTTATGGTAC
Sequence-based reagent	LoxP Oligo reverse	Integrated DNA Technology		CATAACTTCGTATAATGTATG CTATACGAAGTTATGCTGAG CAGATC
Sequence-based reagent	genotyping	Integrated DNA Technology		GAGGAAGCAAAGTGTGTCAGC

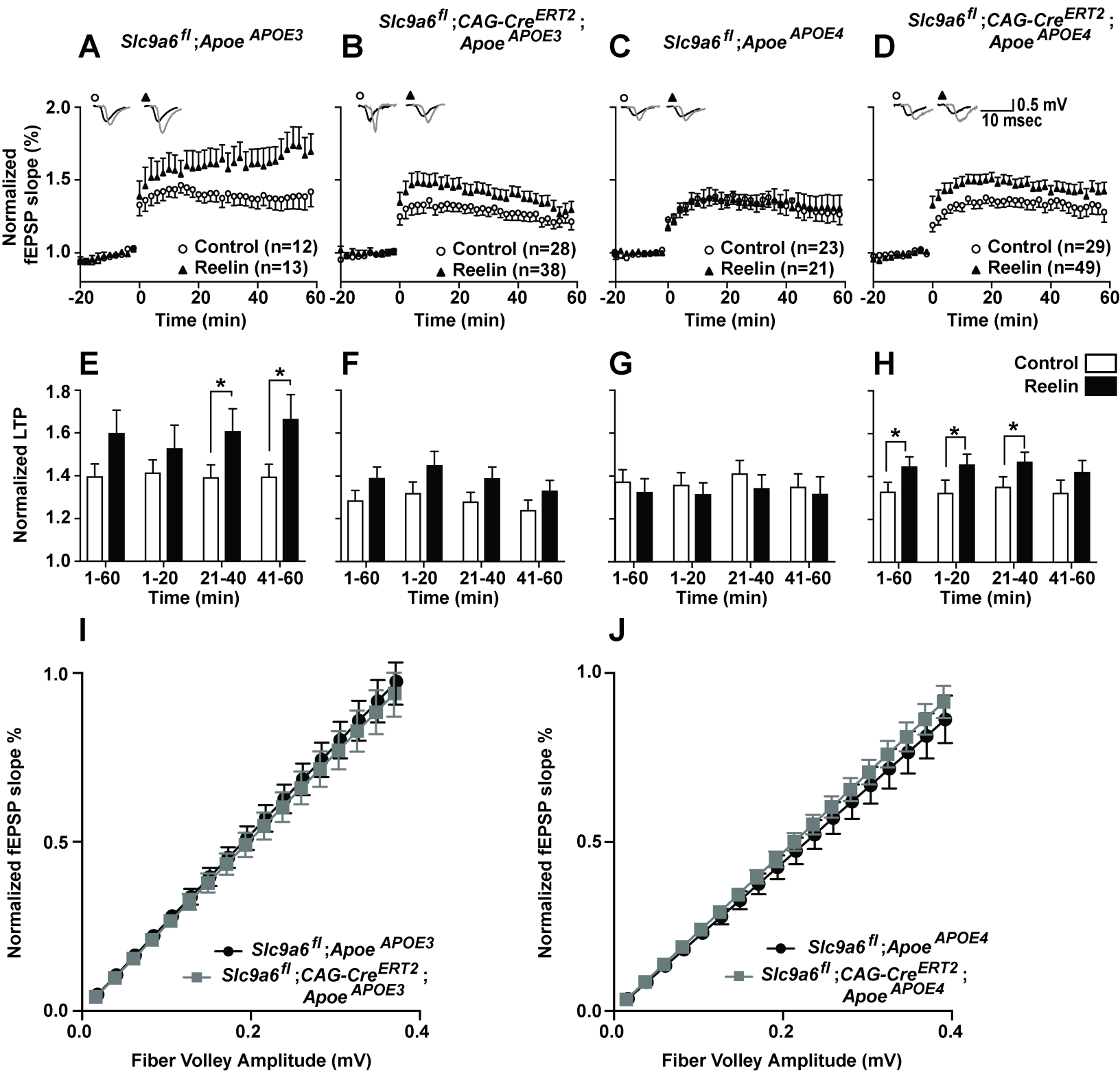
reagent	NHE6-floxed and wt forward	Technology		TCC
Sequence-based reagent	genotyping NHE6-floxed and wt reverse	Integrated DNA Technology		CTAATCCCCTCGGATGCTGC TC
Sequence-based reagent	genotyping NHE6-KO forward	Integrated DNA Technology		GAGGAAGCAAAGTGTGAGC TCC
Sequence-based reagent	genotyping NHE6-KO reverse	Integrated DNA Technology		CCTCACAAGACTAGAGAAAT GGTTC
Sequence-based reagent	Vamp3 forward	Integrated DNA Technology		TTCAAGCTTCACCATGTCTA CAGGTGTGCCTTCGGGGTC
Sequence-based reagent	Vamp3 reverse	Integrated DNA Technology		CATTGTCATCATCATCATCG TGTGGTGTGTCTCTAAGCTG AGCAACAGCGCCGTGGACG GCACCGCCGGCCCCGGCAG CATCGCCACCAAGCTTAAC
Sequence-based reagent	pHluorin2 forward	Integrated DNA Technology		CCGGTCCCAAGCTTATGGTG AGCAAGGGCGAGGAGCTGT TC
Sequence-based reagent	pHluorin2 reverse	Integrated DNA Technology		GCCCTCTTCTAGAGAATTCA CTTGTACAGCTCGTCCATGC CGTG

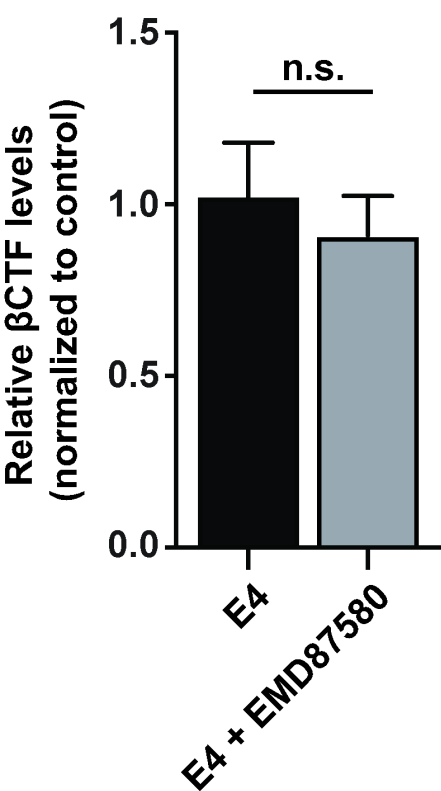
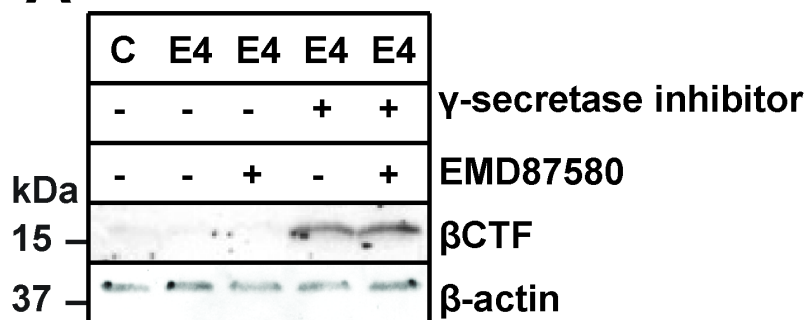


**A****B****C****D****E****F****G**







**A****B**